Lithos 376–377 (2020) 105795

Contents lists available at ScienceDirect

Lithos

journal homepage: www.elsevier.com/locate/lithos

Research Article

# Middle Paleozoic intermediate-mafic rocks of the Tsoroidog Uul' accretionary complex, Central Mongolia: Petrogenesis and tectonic implications

Lkhagvasuren Dagva-Ochir [a,b], Tumen-Ulzii Oyunchimeg [b], Batkhuyag Enkhdalai [b], Inna Safonova [c,d], Huan Li [a,*], Dorjsuren Otgonbaatar [b], Landry Soh Tamehe [a], Davaanyam Sharav [b]

[a] Key Laboratory of Metallogenic Prediction of Nonferrous Metals and Geological Environment Monitoring, Ministry of Education, School of Geosciences and Info-Physics, Central South University, Changsha 410083, China
[b] Institute of Geology, Mongolian Academy of Sciences, Labor Union St., Ulaanbaatar, Mongolia
[c] Sobolev Institute of Geology and Mineralogy SB RAS, Koptyugaave. 3, Novosibirsk, Russia
[d] Novosibirsk State University, Pirogova St. 2, Novosibirsk, Russia

ARTICLE INFO

*Article history:*
Received 9 April 2020
Received in revised form 15 September 2020
Accepted 19 September 2020
Available online 23 September 2020

*Keywords:*
Khangay-Khentey
Ocean Plate Stratigraphy
Accretionary complex
Major and trace elements
Nd isotopes

ABSTRACT

The Tsoroidog Uul' accretionary complex is hosted by the Tsetserleg terrane in the southwestern Khangay-Khentey orogenic system (Central Mongolia), which represents the segment of the Central Asian Orogenic Belt and has significant regional implications for its tectonic evolution. This paper reports the results of field investigations and petrography, bulk-rock major and trace element geochemical, as well as Sm—Nd isotopes of Middle Paleozoic intermediate-mafic rocks from the Tsoroidog Uul' accretionary complex. We investigate a wide range of rock types which can be divided into 4 groups on the basis of their $TiO_2$ and REE characteristics. Group 1 is characterized by moderate $TiO_2$, relatively flat chondrite-normalized REE patterns ($La/Sm_n = 1.0$; $Gd/Yb_n = 1.2$). These basalts are divided into two subgroups: (1) $Nb/Th_{pm} = 3.6$, $Nb/La_{pm} = 0.8$, $Zr/Nb = 24.6$, and $Ce/Yb_{pm} = 0.8$ (N-MORB type); (2) $Nb/Th_{pm} = 1.3$, $Nb/La_{pm} = 1.1$, $Zr/Nb = 11.9$, and $Ce/Yb_{pm} = 1.6$ (*E*-MORB type). Group 2 shows high $TiO_2$ and LREE ($La/Sm_n = 3.0$), differentiated HREE ($Gd/Yb_n = 2.5$), positive Nb anomalies shown in primitive mantle-normalized multi-element patterns ($Nb/Th_{pm} = 1.2$; $Nb/La_{pm} = 1.1$), and low $Zr/Nb_{av.}$ ratios (~6). Group 3 displays low $TiO_2$, high LREE ($La/Sm_n = 3.6$), $Zr/Nb_{av.} = 24.4$, and low Nb ($Nb/La_{pm} = 0.2$). Group 4 exhibits moderate $TiO_2$, flat REE patterns ($La/Sm_n = 0.8$; $Gd/Yb_n = 1.1$), negative Nb anomalies ($Nb/Th_{pm} = 0.3$; $Nb/La_{pm} = 0.6$) and $Zr/Nb_{av.} = 33$. The εNd(t) values are positive for Group 1 and Group 2, but negative for Group 3. Based on their petrological and geochemical features, we suggest that the Group 1 and 2 mafic volcanic rocks were formed in an oceanic environment, and represent mid-oceanic ridge basalt (MORB) and oceanic-island basalt (OIB), respectively. In contrast, Group 3 intermediate dikes probably have supra-subduction origin with calc-alkaline features, whereas Group 4 represents arc tholeiite basalt including remnants of the continental volcanic arc. Overall, the Middle Paleozoic intermediate-mafic rocks of the Tsoroidog Uul' accretionary complex were probably generated from heterogenous mantle sources. Thus, we propose that spatial and temporal changes of the Paleo-Pacific Oceanic lithosphere, which subducted under the continental margin of the Siberian Craton, resulted in the variable composition of the intermediate-mafic rocks of this complex. The accretionary complex of the Tsetserleg terrane, which extends into Ulaanbaatar terrane, was formed by subduction of the Paleo-Pacific Oceanic lithosphere or Mongol-Okhotsk Ocean.



## 1. Introduction

The Central Asian Orogenic Belt (CAOB) (Fig. 1a) is one of the largest orogenic systems on Earth and extends from the Ural Mountain to the Pacific Ocean and from Siberian craton to the Tarim and Sino-Korean Cratons (Zorin, 1999; Badarch et al., 2002; Khain et al., 2002; Jahn, 2004; Xiao et al., 2004; Windley et al., 2007).This orogenic belt was formed by the accretion of island arcs, ophiolites, oceanic islands, seamounts, accretionary wedges, oceanic plateaus and microcontinents. However, the tectonic evolution of the CAOB remains debated with three different models including: (1) strike-slip duplication and oroclinal bending of a giant magmatic arc (Şengör et al., 1993); (2) successive accretion of oceanic and continental terranes to the Siberian craton (Badarch et al., 2002; Windley et al., 2007), and (3) two stages of evolution involving the Pacific-type accretion during the Devonian-Carboniferous, followed

* Corresponding author.
*E-mail address:* lihuan@csu.edu.cn (H. Li).

https://doi.org/10.1016/j.lithos.2020.105795
0024-4937/

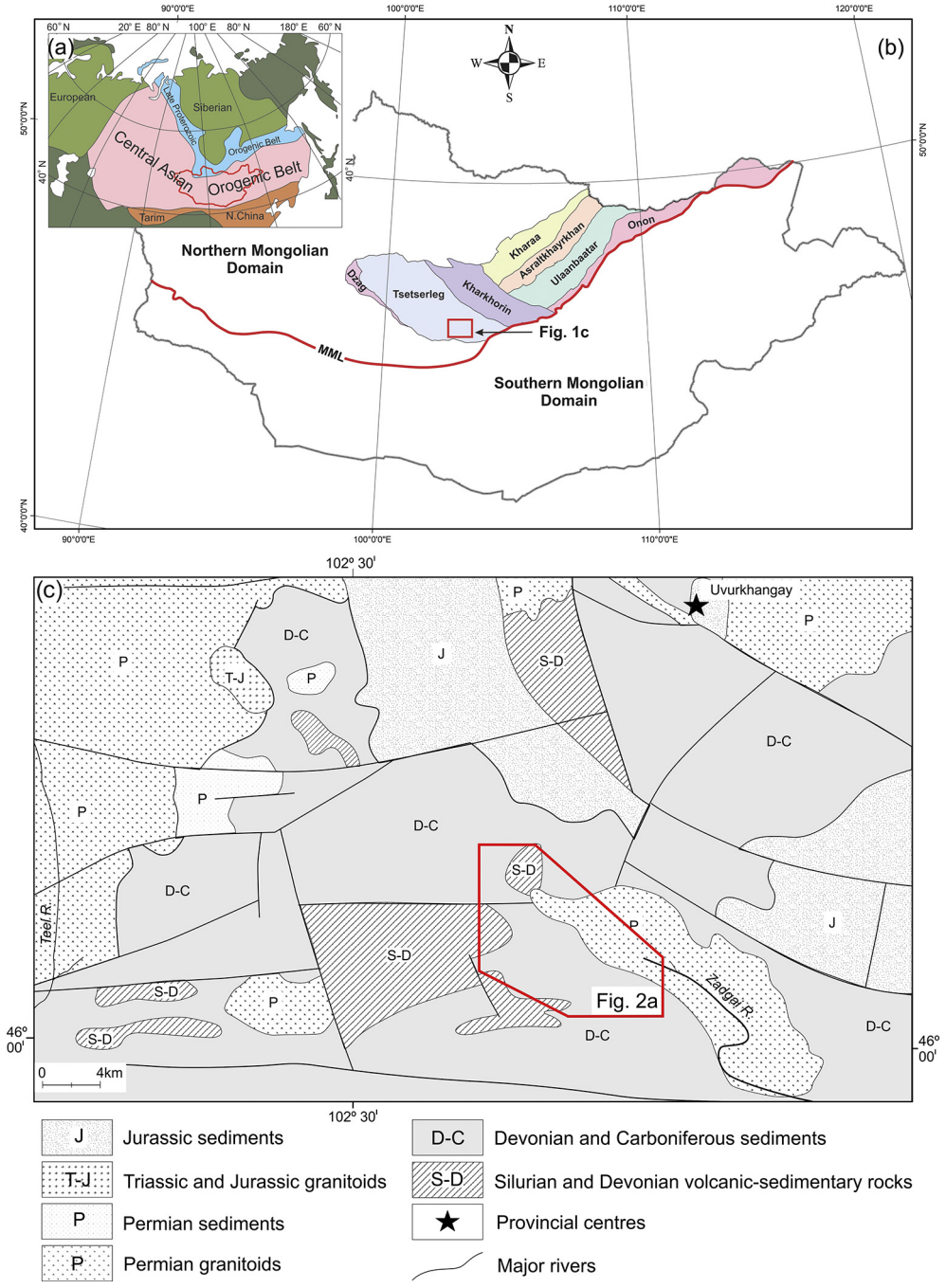


**Fig. 1.** (a) Main tectonic units of the Central Asian Orogenic Belt (CAOB) (modified after Jahn, 2004), showing the location of Mongolia in the frame of the Asian continent and the CAOB. (b) Mongolian tectonostratigraphic map (modified after Tomurtogoo 2012), showing the location of the Khangay-Khentey orogenic system. (c) Simplified geological map of the Tsetserleg terrane (modified after Tomurtogoo et al., 2017).

by the Tethysian-type oroclinal bending and collisional shortening during the Permian to Jurassic (Lehmann et al., 2010; Schulmann and Paterson, 2011). Nonetheless, recent studies regarding the stratigraphy, petrology, structural geology, geochemistry, and geochronology of diverse units from the CAOB have greatly developed our understanding of the processes that control its global tectonic and continental growth (e.g., Jahn et al., 2000a, 2000b, Jahn, 2004; Xiao et al., 2003, 2004; Kovalenko et al., 2004; Windley et al., 2007; Yarmolyuk et al., 2008; Safonova et al., 2009; Wilhem et al., 2012; Yarmolyuk et al., 2012; Kovach et al., 2013; Safonova and Santosh, 2014).

The Mongolia region (Fig. 1a) occupies a large part of the CAOB and has been divided into two main domains known as Northern Mongolian and Southern Mongolian (Badarch et al., 2002; Tomurtogoo, 2003, 2012). The Southern Mongolian domain is located within the northern orogenic belt of the North China and Tarim Cratons, which is dominated by Neoproterozoic to Paleozoic sedimentary rocks, arc-related volcanic and volcaniclastic rocks with ophiolite fragments. These basement rocks are covered by Middle Paleozoic carbonate rocks and a variety of post-Paleozoic volcanic and sedimentary rocks (Badarch et al., 2002; Tomurtogoo, 2003). In contrast, the Northern Mongolian domain

belongs to the southern orogenic belt of Siberian craton, which consists of Archean–Proterozoic cratonic blocks, Neoproterozoic to Lower Paleozoic metamorphic rocks and ophiolites, and Paleozoic volcanic and sedimentary rocks (Badarch et al., 2002). They are widely intruded by Paleozoic to Mesozoic granitic rocks. The Khangay-Khentey orogenic system (also known as Khangai-Khentei and Khangai-Khantey in some literatures) is located in the central part of the Northern Domain (Fig. 1b; Tomurtogoo, 2005, 2012). This orogenic system consists of the Khangay and Khentey mountain ranges, and is about 300 km wide and 1200 km long (Tomurtogoo, 2003). Several different tectonic settings have been proposed to explain the formation of the Khangay-Khentey orogenic system, which include: (1) miogeosyncline basin corresponding to a Devonian–Carboniferous thick turbidite basin probably deposited on a hidden Archean–Neoproterozoic basement (Badarch et al., 2002; Badarch, 2005), (2) oceanic turbidite terranes (Tomurtogoo, 2003), and (3) accretionary complex (Şengör and Natal'in, 1996; Zorin, 1999; Kurihara et al., 2009; Safonova et al., 2009; Hara et al., 2013; Tomurtogoo, 2005, 2012; Tsukada et al., 2013; Safonova and Santosh, 2014). The Khangay-Khentey orogenic system comprises diverse terranes such as the Zag-Kharaa turbidite terrane and the Asraltkhayrkhan, Kharkhorin, Tsetserleg, Ulaanbaatar, and Onon accretionary terranes (Tomurtogoo, 2005, 2012). Based on detrital zircon geochronological and micropaleontological studies of the Paleozoic sedimentary rocks from the Tsetserleg and Ulaanbaatar terranes, numerous researchers have identified their provenance and depositional age, and proposed a geodynamic model for the Khangay-Khentey orogenic system (Kelty et al., 2008; Kurihara et al., 2009; Bussien et al., 2011; Purevjav and Roser, 2012, 2013; Suzuki et al., 2012; Takeuchi et al., 2012; Hara et al., 2013; Erdenechimeg et al., 2018). However, the tectonic evolution of this orogenic system is still unresolved.

The Tsetserleg terrane is located in the southwestern part of the Khangay-Khentey orogenic system (Fig. 1b), which mainly consists of Devonian and Carboniferous siliceous sedimentary rocks (Purevjav and Roser, 2012) and oceanic volcanic rocks (Erdenesaikhan et al., 2013; Tsukada et al., 2013) (Fig. 1c). Previous studies were mainly focused on the geochemistry and geochronology of the Paleozoic sedimentary rocks from the Tsoroidog Uul' accretionary complex (TUAC), which is considered to be the most important complex of the Tsetserleg terrane (Oyunchimeg et al., 2018). In contrast, the geochemical compositions of the oceanic volcanic rocks from this complex have been briefly reported in the literature (Oyunchimeg et al., 2017). Since basalts that originate from oceanic environments are extremely important for understanding the reconstruction of different geodynamic settings (Safonova et al., 2008, 2011a, 2011b, 2012; Saccani and Principi, 2016, Saccani et al., 2018; Safonova et al., 2020), more research should be addressed on such rock types of the TUAC. Thus, we present the first detailed petrographic, geochemical and Sm—Nd isotopic studies of the intermediate-mafic rocks from the Tsetserleg terrane. All these data are used to constrain the petrogenesis, mantle sources, and tectonic settings of the studied rocks. These new data further allow us to unravel the tectonic evolution of the Khangay-Khentey orogenic system.

## 2. Geology of the Tsoroidog Uul' accretionary complex

### 2.1. Geological background

The TUAC is located in the southeastern part of the Tsetserleg terrane (Fig. 1b), which has a length of 30 km and a width of 25 km. The Tsetserleg terrane is bordered by the Galuut fault along the southern side with the Zag terrane and the Baidrag uplift, the Kharkhorin fault along the northeastern side with the Kharkhorin terrane, and the Mid Mongolian Tectonic fault along the southeastern side with the Southern Mongolian domain (Badarch et al., 2002; Bussien et al., 2011; Kelty et al., 2008; Shevchenko et al., 2014; Tomurtogoo, 2005).

The thickish siliceous-terrigenous sediment of the Tsetserleg terrane was first named "Khangay Group" (Ufland and Filippova, 1967) and consists of Lower–Middle Devonian Erdenetsogt Formation, Middle–Upper Devonian Tsetserleg Formation, and Lower Carboniferous Jargalant Formation. Kurihara et al., (2009) reported clear evidence for an accretionary complex origin of sediments from the Gorkhi Formation in the Ulaanbaatar terrane and correlated them into the Erdenetsogt formation in the Tsetserleg terrane, whereas the Tsetserleg and Jargalant Formations are interpreted as shallow marine cover sediments accumulated over the accretionary complex (Kurihara et al., 2009) in the tectonic setting of fore-arc basins (Bussien et al., 2011). Based on our field investigations, geochemical, geochronological and micropaleontological data (Fig. 2a, b), we reclassified the lithofacies of the Middle to Late Paleozoic units in the TUAC using the theory of Ocean Plate Stratigraphy (Isozaki, 1997), however, we keep the formation names of the "Khangay Group" to avoid any confusion. The TUAC was intruded by granitoids of the Khangay Complex (granodiorite, diorite, granite) during Permian (Orolmaa et al., 2008; Togtokh et al., 1986). This region overall comprises volcanic and subvolcanic rocks (basalts and basaltic andesites), pelagic sediments (cherts), hemipelagic sediments (siliceous mudstones, siltstones and shales) and trench sediments (turbidites, sandstones and conglomerates) (Fig. 2).

### 2.2. Stratigraphy of the TUAC

As mentioned above, there are three main stratigraphic units exposed in the Khangay Group, which include in ascending order: the Erdenetsogt Formation, the Tsetserleg Formation, and the Jargalant (Dzargalant) Formation (Fig. 2a). The ages of these formations were mainly obtained by faunas and fossils (Togtokh et al., 1986). In this study, we redefined the sequences of those formations using modern research approach.

The Tsetserleg Formation is characterized by turbidite sequence consisting of medium-to coarse-grained clastic rocks dated at 382-337 Ma (LA-ICP-MS U—Pb on zircon; Erdenechimeg et al., 2018). The Jargalant Formation is represented by mudstones and siltstones associated with some fine- to medium-grained clastic rocks and conglomerates, which recorded ages of 330–300 Ma (LA-ICP-MS U—Pb on zircon; Oyunchimeg et al., 2018). In contrast, the Erdenetsogt Formation mainly consists of basaltic lava, basaltic pyroclastic rocks, breccias, minor limestones, dark-brownish metacherts, whitish-gray to brown-reddish cherts, siliceous siltstones and shales. The latter rock sequences were dated at Middle Silurian to Upper Devonian based on radiolarian analyses (Fig. 3a, b) and lithostratigraphic correlations (Fig. 2b; Kurihara et al., 2009; Hara et al., 2013). Stratigraphic units are crosscut by intermediate dikes such as andesite and basaltic andesite (Fig. 2a). The rock sequences of these stratigraphic units are consistent with the OPS model or succession (basalt–chert–siliceous mudstone/siltstone–sandstone) (Isozaki, 1997; Maruyama et al., 2010; Safonova et al., 2016, 2020). Thus, the Erdenetsogt Formation can be regarded as the lower to middle OPS unit (pelagic plus hemipelagic), whereas the Tsetserleg and Jargalant Formations correspond to the upper OPS unit. Overall, the Erdenetsogt Formation is mainly composed of oceanic plate rocks, whereas the Tsetserleg and Jargalant Formations are lithologically similar and dominated by flyshoid and turbidite sequences. It should be noted that these three Formations are correlated with the Mesozoic Ocean Plate Stratigraphy in Japan in terms of lithological association (Isozaki, 1997).

### 2.3. Geological features of the Erdenetsogt Formation

For this study, two cross-sections (cross-section 1: N45°56′10.2″, E102°43′17.4″; and cross-section 2: N46°03′6.9″, E102°33′56.3″) of the Erdenetsogt Formation were investigated in detail (Fig. 4). The Erdenetsogt Formation can be divided into three subunits. The lower subunit crops out at the Mount Ikh Avzaga and consists of thick-

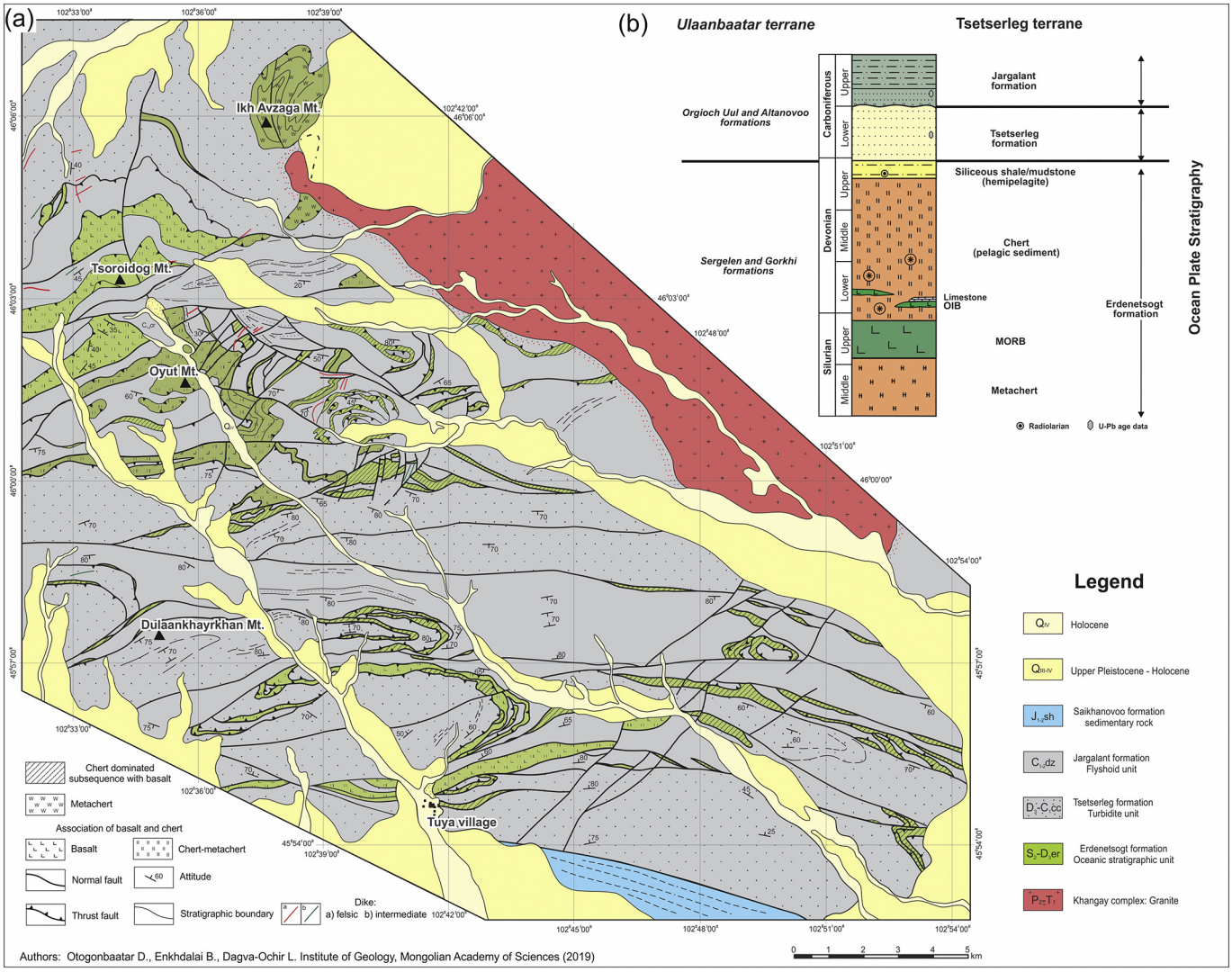


**Fig. 2.** (a) Geological map of the Tsoroidog Uul' accretionary complex. (b) Lithostratigraphic column of the Tsoroidog Uul' accretionary complex.

bedded dark-gray colored metacherts with a few layers of greenschist facies metamorphosed basalts. These rocks are strongly deformed at mesoscale as they are clearly folded. The middle subunit is widely distributed in the central part of the Erdenetsogt Formation and mainly comprises brown-gray and whitish-gray colored chert-metachert, brownish-red colored tuffaceous shale/ash tuffs, and mafic volcanic

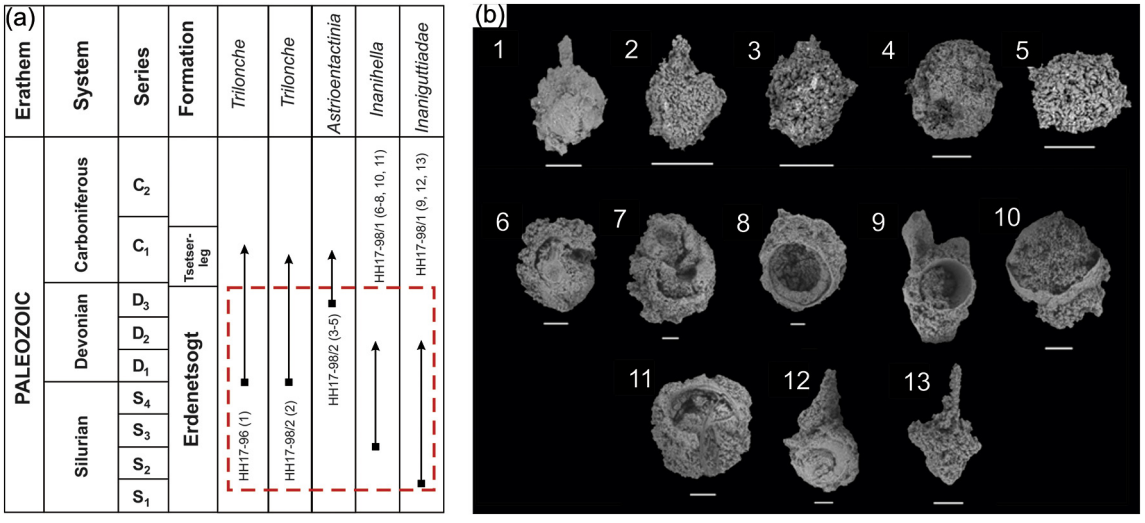


**Fig. 3.** (a) Vertical distribution of the radiolarians in the Erdenetsogt Formation; (b) Radiolarians from the Erdenetsogt Formation. All scale bars represent 100 μm.

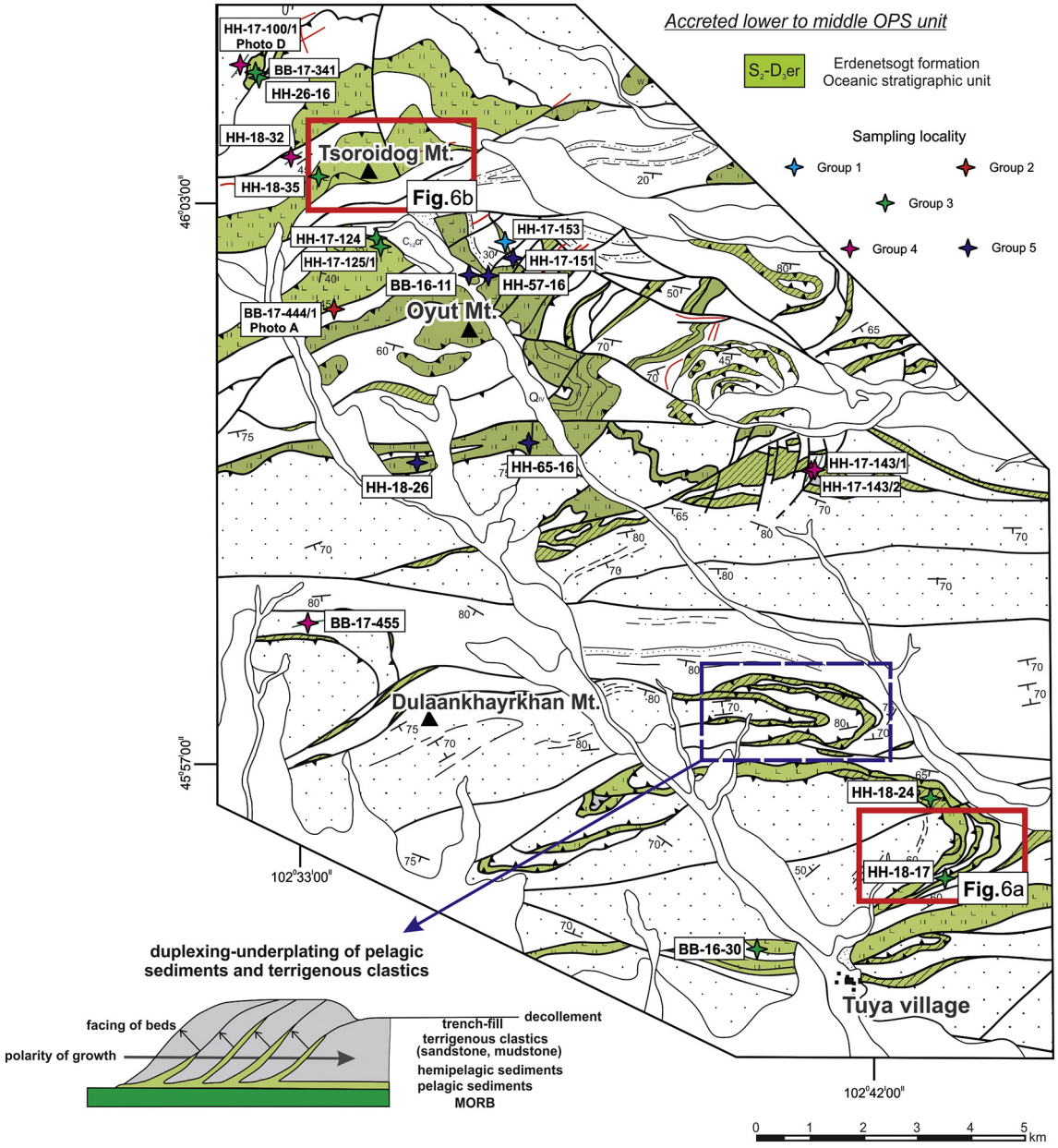


**Fig. 4.** Geological map of the lower to middle OPS unit from the Erdenetsogt Formation in the Tsoroidog Uul' accretionary complex, showing the sample locations.

rocks. The upper subunit is composed of thin-bedded, red and red-brown colored cherts, minor bluish-gray and dark-gray tuffaceous sediments, and gray-greenish siliceous shales. The red cherts contain Middle–Upper Devonian radiolarians (Oyunchimeg et al., 2018). Generally, positions of outcrops in the field allow us to recognize that units of the TUAC can be identified by chaotic rock assemblages that include numerous blocks/lenses of various lithology (Isozaki, 1997). However, the coherent-type unit, which comprises two distinct lithologic units, is rarely revealed in the study area and is represented by bedded radiolarian chert and clastic rocks such as sandstone and mudstone (Fig. 4).

Detailed investigations of the above cross-sections yielded more structural features for the Erdenetsogt Formation. The cross-section 1 is observed on a synclinal structure in the southern part of the study area, where the Erdenetsogt Formation is bounded by the Tsetserleg Formation turbiditic sandstone and Jargalant Formation flyshoid sediments (Fig. 5a). Cross-section 2 is exposed at Mount Tsoroidog and reveals that the Erdenetsogt Formation is principally separated from the Jargalant Formation thick massive sandstone by faults (Fig. 5b). In both cross-sections, the thrusting-related deformation is revealed by some sheared basalt, chert and siliceous shale, as well as by the presence of large chert boudins within basalts. The chert and siliceous shale are often in direct contact with underlying basalt showing thrusting, folding and shearing features.

## 3. Samples and analytical methods

### 3.1. Sampling strategy

Over 80 volcanic and subvolcanic rock samples (mainly mafic volcanic and intermediate-mafic subvolcanic rocks (Fig. 6a–h), were collected from the chert-basalt sequences of the Erdentsogt Formation around the Mount Oyut, Mount Tsoroidog, and Tuya village. The sample descriptions are summarized in Table 1 and their lithostratigraphic positions are shown in Fig. 2b.

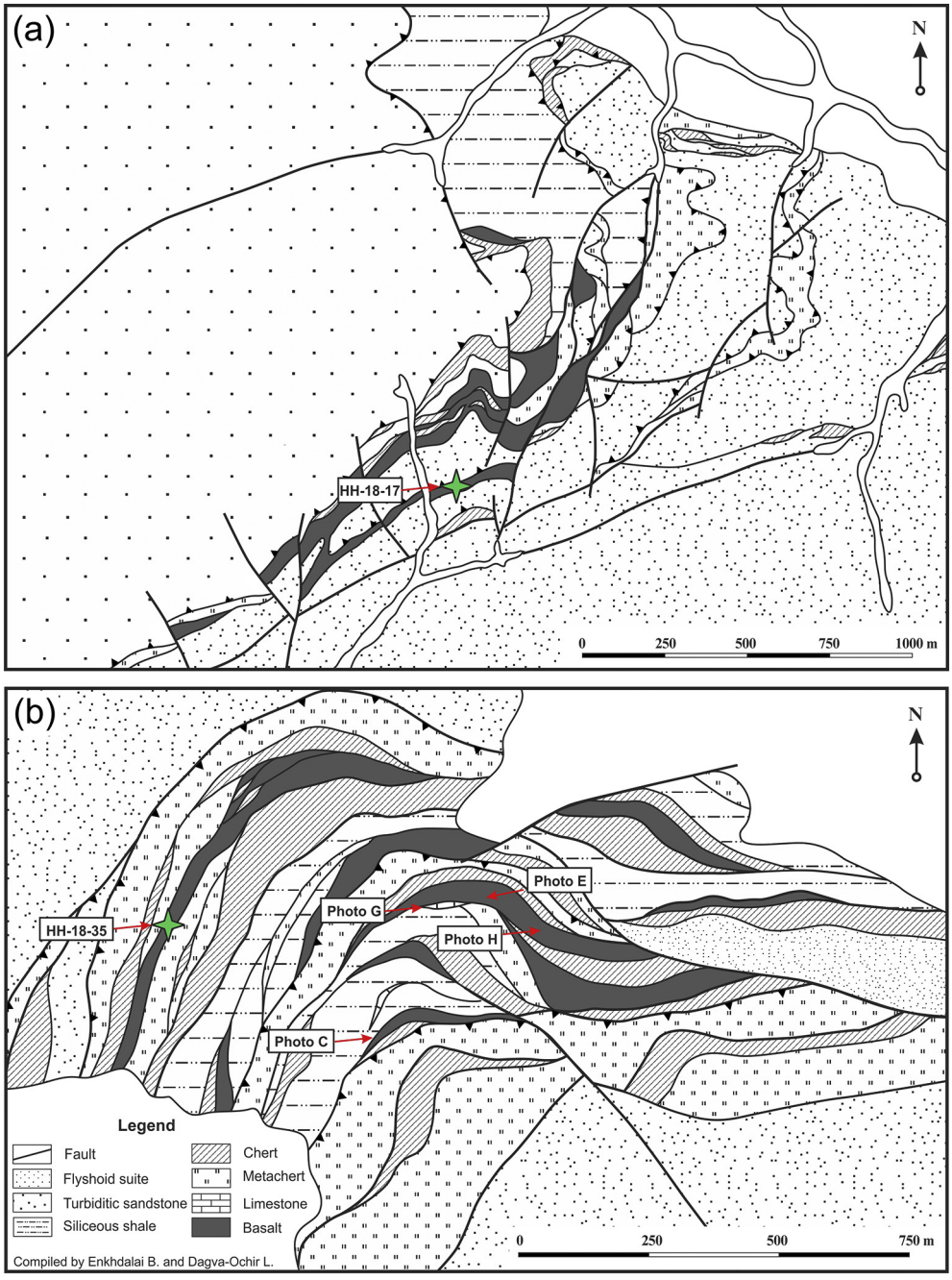


**Fig. 5.** Overturned/folded duplex structures in the Tsoroidog Uul' accretionary complex: (a) northern and (b) southern parts.

Petrographic analysis and sample preparation for geochemical studies were performed at the Institute of Geology, Mongolian Academy of Sciences. Based on field investigations and microscopic studies, we infer that the volcanic and subvolcanic rocks taken from the TUAC only underwent weak secondary alteration and weak weathering. Thus, the results of geochemical analyses are reliable for the petrogenetic interpretation.

### 3.2. Major and trace element geochemistry

A total of 22 intermediate-mafic rocks taken from the TUAC were analyzed for major and trace element at SGS Mongolia (invested by Switzerland), using standard procedure (https://www.sgs.mn). Samplesselected for the analyses were checked under microscope and the freshest parts of the rocks were crushed into powder. Major element concentrations were analyzed by X-ray Fluorescence Spectrometry (XRF) and trace element concentrations by Inductively-Coupled Plasma Mass Spectrometry (ICP-MS) using the glass bead method. For the major element analysis, glass beads were prepared by fusing mixtures of 0.7 g of powdered sample with 6.0 g of lithium tetraborate. For the trace element analysis, 2.0 g of powdered sample was fused with 4.0 g of lithium tetraborate. Data management, re-calculation and plotting were estimated using *Grapher 9.6* software (https://www.goldensoftware.com/products/grapher).

### 3.3. Sm—Nd isotopic analysis

The Sm—Nd isotopic analysis was performed at the Geological Institute of the Kola Science Center, Russian Academy of Sciences. The Sm—Nd isotope measurements were performed using a Finnigan

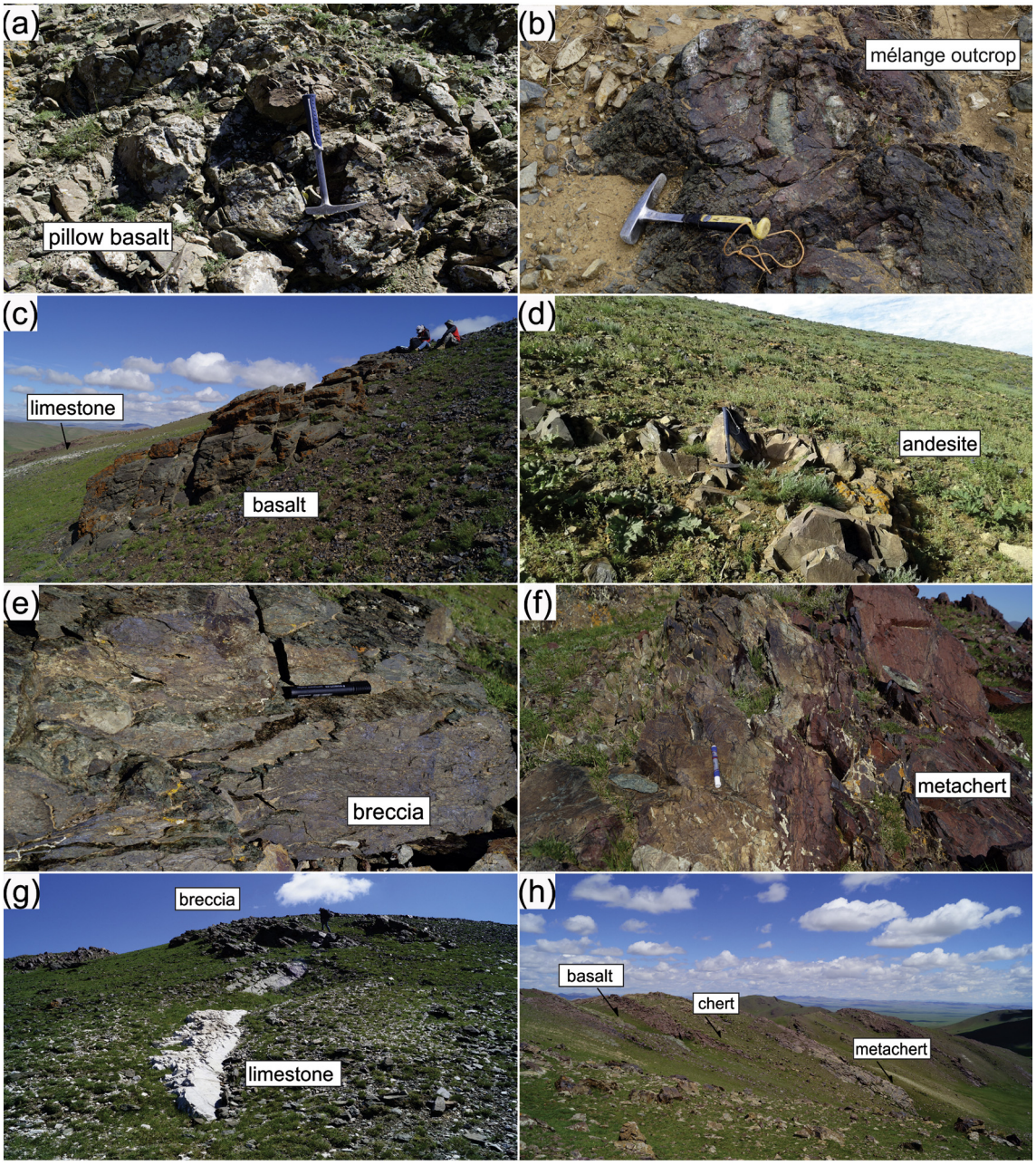


**Fig. 6.** Field photos of outcrops from the Tsoroidog Uul' accretionary complex. (a) pillow basalt, (b) mélange outcrop, (c) basalt and limestone, (d) andesite, (e) breccia, (f) metachert, (g) limestone and breccia, (h) contact between basalt, chert and metachert.

MAT 262 mass spectrometer in static mode. Rock powders were dissolved in a mixture of HF, $HNO_3$ and $HClO_4$. Before decomposition, all samples were spiked with a mixed $^{149}Sm/^{150}Nd$ solution. The REEs were separated using conventional cation-exchange techniques. The Sm and Nd were separated by extraction chromatography in Eichrom LN-Specres in columns. Blanks in the laboratory were 0.1–0.2 ng for Sm and 0.1–0.5 ng for Nd. The Sm and Nd contents were measured to an accuracy of ±0.5%, and their ratios were accurate to ±0.5% for $^{147}Sm/^{144}Nd$ and ± 0.005% for $^{143}Nd/^{144}Nd$ (2σ). The $^{143}Nd/^{144}Nd$ ratios were normalized to the value of the La Jolla standard (0.511860). During the analyses, the weighted averages of nine La Jolla Nd-standard runs yielded 0.511852 ± 8 (2σ) for $^{143}Nd/^{144}Nd$, and the value of 0.7219 was used to normalize $^{146}Nd/^{144}Nd$. The εNd(t) values were calculated using the present-day values for a chondritic uniform reservoir (CHUR) of $^{143}Nd/^{144}Nd = 0.512638$ and $^{147}Sm/^{144}Nd = 0.1967$ (Jacobsen and Wasserburg, 1984). The TDM model ages were calculated with reference to the model of Goldstein and Jacobsen (1988), assuming that the Nd isotope composition of depleted mantle has evolved linearly since 4.56 Ga and is currently εNd(0) = +10 ($^{143}Nd/^{144}Nd = 0.513151$ and $^{147}Sm/^{144}Nd = 0.2137$). The two stage Nd model ages, tDM2 (Keto and Jacobsen, 1987), were calculated using the crustal mean ratio of $^{147}Sm/^{144}Nd = 0.12$ (Taylor and McLennan, 1985).

## 4. Results

### 4.1. Petrography

Most of the studied rock samples were affected by secondary alteration as shown by replacement of primary minerals. For instance, plagioclase is rarely replaced by albite, whereas clinopyroxene is occasionally pseudomorphosed either by chlorite or actinolitic amphibole. Nevertheless, it should be noted that primary igneous textures in

**Table 1**
Description of intermediate-mafic rock samples from the Tsoroidog Uul' accretionary complex.

| Group/Sample no. | Rock type | Mode of occurrence | Location | Coordinates |
|---|---|---|---|---|
| Group 1 | | | | |
| HH-17-153 | Basalt | Lava flow | Oyut Mt. | 102°36′13.1″E; 46°02′30.1″N |
| BB-17-444/1 | Basalt | Pillow-lava | Oyut Mt. | 102°36′32.1″E; 46°00′19.2″N |
| Group 2 | | | | |
| HH-17-124 | Trachybasalt | Lava flow | Oyut Mt. | 102°34′09.5″E; 46°02′34.2″N |
| BB-17-341 | Basalt | Lava flow | Tsagaan Zalaa Mt. | 102°32′16.4″E; 46°04′22.2″N |
| HH-26-16 | Basalt | Lava flow | Tsagaan Zalaa Mt. | 102°32′23.2″E; 46°04′17.6″N |
| BB-16-30 | Basalt | Lava flow | TuyaVlg. | 102°40′06.3″E; 45°54′56.3″N |
| HH-18-35 | Basanite | Lava flow | Tsoroidog Mt. | 102°33′19.3″E; 46°03′21.9″N |
| HH-17-125/1 | Pyroxene-porphyrite | Lava flow | Oyut Mt. | 102°34′12.1″E; 46°02′29.4″N |
| HH-18-24 | Picrobasalt | Lava flow | TuyaVlg. | 102°42′42.4″E; 45°56′30.5″N |
| HH-18-17 | Picrobasalt | Lava flow | TuyaVlg. | 102°42′53.8″E; 45°55′43.6″N |
| Group 3 | | | | |
| HH-17-100/1 | Trachyandesite | Dike | Tsagaan Zalaa Mt | 102°32′05.2″E; 46°04′27.8″N |
| HH-17-143/1 | Basaltic trachyandesite | Dike | NamsraynOvoo Mt. | 102°41′04.0″E; 46°00′08.4″N |
| HH-17-143/2 | Basaltic trachyandesite | Dike | NamsraynOvoo Mt. | 102°41′03.9″E; 46°00′08.3″N |
| BB-17-455 | Basaltic andesite | Dike | Dulaankhayrkhan Mt. | 102°33′05.3″E; 45°58′19.5″N |
| HH-18-32 | Basaltic trachyandesite | Dike | Tsoroidog Mt. | 102°32′45.6″E; 46°03′23.5″N |
| Group 4 | | | | |
| HH-17-151 | Basalt | Lava flow | Oyut Mt. | 102°36′16.4″E; 46°02′23.5″N |
| HH-18-26 | Basalt | Lava flow | Shar Tsohoi Mt. | 102°34′39.3″E; 46°00′07.3″N |
| HH-141-16 | Basalt | Lava flow | SonduultUul Mt. | 102°24′38.1″E; 45°58′12.6″N |
| HH-65-16 | Basalt | Lava flow | Shar Tsohoi Mt. | 102°36′32.1″E; 46°00′19.2″N |
| BB-16-11 | Basalt | Lava flow | Oyut Mt. | 102°35′34.7″E; 46°02′08.5″N |
| HH-121-16 | Basalt | Lava lava | Arvaikheer Prov. | 102°40′16.0″E; 46°14′12.3″N |
| HH-57-16 | Basalt | Lava flow | Oyut Mt. | 102°35′53.8″E; 46°02′08.8″N |

these rocks are well preserved. The volcanic rocks are generally composed of aphyric, porphyritic, olivine basalts and weakly metamorphosed basalts, whereas the subvolcanic rocks comprise amphibole-bearing and plagioclase-bearing porphyritic basalts, diabases and basaltic andesites (Table 1; Fig. 7a–f).

Most of these rock samples display porphyritic and aphyric texture and massive or, not often, amygdaloidal structure. The porphyritic basalt, a representative sample is HH-18-24 (Fig. 7f), contains mainly clinopyroxene (30–35%) and amphibole (50–55%) as its phenocrysts, and secondary minerals such as actinolite, epidote, chlorite and carbonate. Groundmass consists of plagioclase (50–55%), volcanic glass (30%) and secondary minerals (10–15%). Clinopyroxene commonly occurs as wide flat and non-isometric phenocrysts (0.03–1.2 mm), and some zoned Ti-augite appears with an extinction angle of 35–40°. Amphibole is generally dark green in color and occurs as stretched flat hexahedral hornblende crystals (0.03–1.0 mm) with an extinction angle of 16-20°. Most of them display a crooked shape probably due to the high pressure, and are partially replaced by chlorite. The secondary minerals often occur along weakened zones and cracks of the rock. Compared to other porphyritic basalt samples, it is noteworthy that sample HH-121-16 contains abundant olivine (20–25%), and less clinopyroxene (5–10%), plagioclase (45–50%) and volcanic glass (10%) (Fig. 7b). Whereas, secondary minerals are sericite, calcite and zeolite. Olivine is whitish green in color and occurs either as anhedral shaped (0.3–0.8 mm) or rare euhedral hexahedral crystals. Generally, olivine phenocrysts are greatly fractured as a result of experiencing highly deformation in the accretionary wedge. Plagioclase appears as stubby laths (0.05–0.65 mm) and partially replaced by zeolite and sericite.

The aphyric basalt, a representative sample is BB-17-444/1 (Fig. 7e), has an amygdaloidal structure. The groundmass displays a variolitic texture, which is caused by the radial orientation of plagioclase. Volcanic glasses replaced by quartz-epidote-actinolite-chlorite and amygdales are filled by zeolite and calcite.

The amphibole-bearing basaltic trachyandesite, a representative sample is HH-18-143/2 (Fig. 7a), has a massive structure and a porphyritic texture comprising abundant plagioclase (50%) and amphibole (50%) phenocrysts, and <5% secondary minerals (epidote, actinolite, chlorite) with minor quartz and opaque minerals. The groundmass shows a hyalopilitic texture containing isotropic volcanic glass. Plagioclase crystals are euhedral long stretched or, not often, stubby laths (0.2–2.0 mm) and partially replaced by epidote. The amphibole is dark greenish yellow in color and occurs as hexahedral hornblende (1.25–2.5 mm) with an extinction angle of 16-18°. It should be noted that a few basaltic andesite samples underwent secondary alteration and sub-greenschist facies of metamorphism, as shown by the chloritization, carbonatization and epidotization in these rocks.

### 4.2. Major and trace element geochemistry

The volcanic and subvolcanic rocks from the TUAC show a wide range of geochemical characteristics, and four geochemical groups can be recognized (Table 2). The Mg# values (Mg# = 100 Mg/(Mg + $Fe^{2+}$) of these rocks vary from 47.2 to 69.7. Large ion lithophile elements (LILE such as Rb, Sr, and Ba) also show wide variations in these samples. Since LILE are highly mobile during post-magmatic alteration, we mainly use high-field strength elements (HFSE) and rare-earth elements (REE), which are less mobile during such process.

Group 1 is represented by basalts on the total alkali-silica diagram (Fig. 8). These rocks showa clear sub-alkaline affinity (Nb/Y ratio = 0.1–0.3, Table 2) and have $Fe_2O_3$ = 10.9–12.2 wt%, $TiO_2$ = 1.7 wt%, $Al_2O_3$ = 13.3–14.5 wt%, MgO = 5.8–6.5 wt%, $P_2O_5$ = 0.1–0.2 wt%, $SiO_2$ = 49.1–49.2 wt% and Mg# = 54.3 (Fig. 9). The Group 1 volcanic rocks are characterized by moderate $TiO_2$ and $Al_2O_3/TiO_2$ ratio of 7.8–8.4. The chondrite-normalized REE diagram of the Group 1 rocks displays relatively flat REE patterns ($La/Yb_n$ = 0.7–1.7), showing low differentation between LREE and HREE ($La/Sm_n$ = 0.7–1.3; $Gd/Yb_n$ = 1.1–1.3) (Fig. 10b). However, these basalts display two different primitive mantle-normalized multi-element patterns (Fig. 10a): (1) $Nb/Th_{pm}$ = 3.6, $Nb/La_{pm}$ = 0.8, $Ce/Yb_{pm}$ = 0.8, and Zr/Nb = 24.6; (2) $Nb/Th_{pm}$ = 1.3, $Nb/La_{pm}$ = 1.1, $Ce/Yb_{pm}$ = 1.6, and Zr/Nb = 11.9.

Group 2 comprises basaltic rock samples that show significant variability of $SiO_2$ = 38.4–48.8 wt%, $Fe_2O_3$ = 9.8–20.3 wt%, $TiO_2$ = 1.9–4.7 wt%, $Al_2O_3$ = 9.9–15.6 wt%, MgO = 4.8–12.3 wt%, $P_2O_5$ = 0.3–1.3 wt%, and Mg# = 49.5–69.7. The Nb/Y ratios (0.7–3.3, Table 2) depict the alkaline character of these samples which dominantly plot in the field of alkali (trachy-) basalts on the total akali-silica diagram

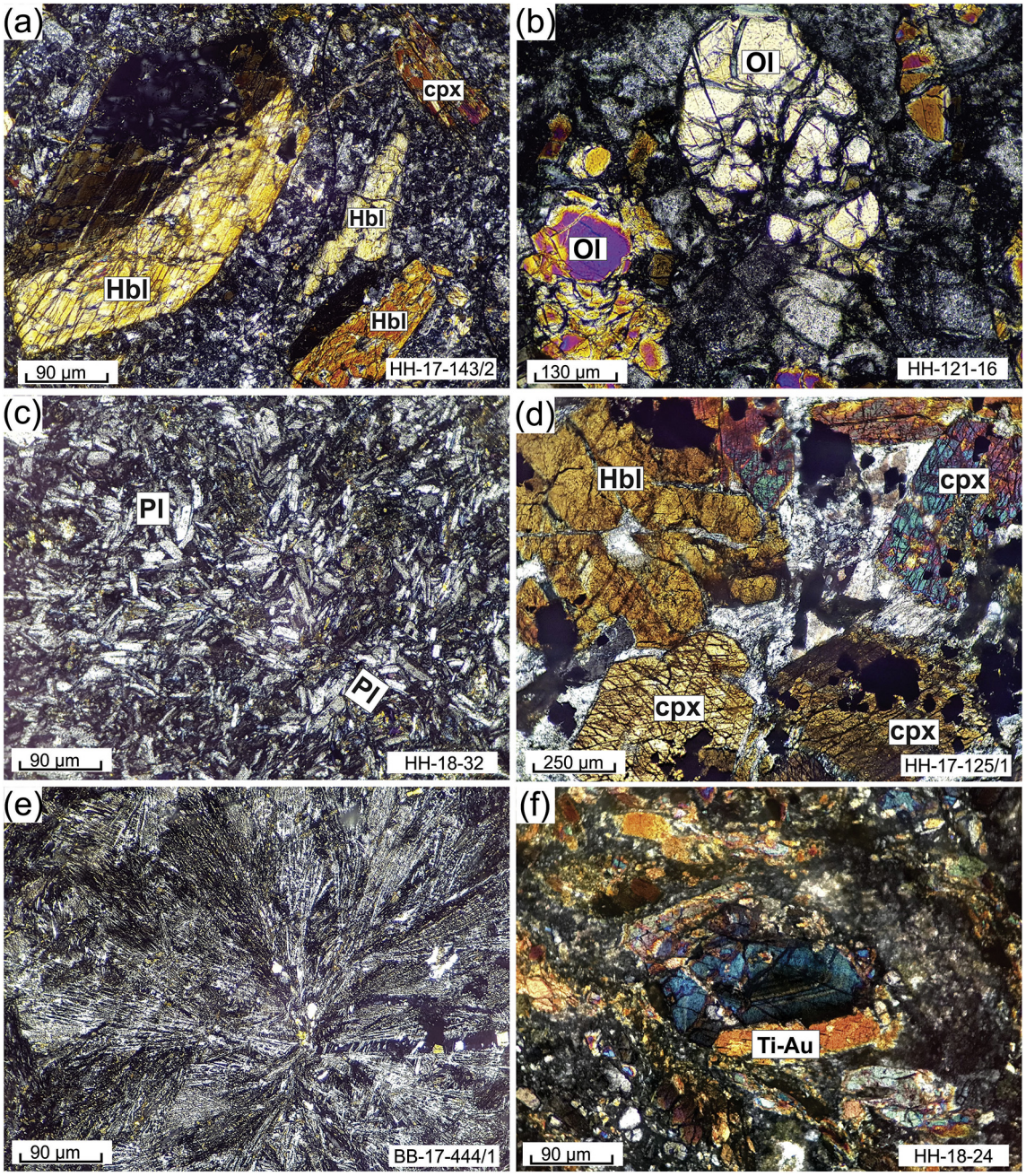


**Fig. 7.** Photomicrographs of representative intermediate-mafic rocks from the Tsoroidog Uul' accretionary complex. (a) basaltic trachyandesite, (b) basalt, (c) basaltic andesite, (d) pyroxene-porphyrite, (e) basalt, (f) picrobasalt. Hbl – hornblende, Ti—Au – titano-augite, Ol – olivine, Cpx – clinopyroxene, Pl – plagioclase.

(Fig. 8). It should be noted that samples HH-17-124 and HH-17-125/1 are characterized by relatively high $TiO_2$ content, low Zr/Nb ratio (6 in average) and $Al_2O_3/TiO_2$ ratio ranging from 2.1 to 8.1 (Table 2).The $TiO_2$ and $Fe_2O_3$ contents show positive correlations with MgO, whereas $Al_2O_3$, $P_2O_5$, Th and Sm are negatively correlated with MgO, and La and Nb are relatively constant with increasing MgO (Fig. 9). The chondrite-normalized REE patterns of Group 2 basaltic rocks display significant LREE enrichment, compared to HREE ($La/Yb_n$ = 4.6–27.3). The degree of LREE and HREE differentiation is moderate to high with $La/Sm_n$ ratio and $Gd/Yb_n$ ratio ranging from 2.0 to 4.1 and from 1.5 to 3.4, respectively (Fig. 10d). The primitive mantle-normalized multi-element patterns show that most of the basaltic rock samples are enriched in incompatible elements and have positive Nb anomalies relative to Th and La ($Nb/La_{pm}$ = 0.7–1.4; $Nb/Th_{pm}$ = 0.5–1.7) (Fig. 10c).

Group 3 intermediate rocks have different major and trace element compositions from the other groups of volcanic rocks. These subvolcanic rocks include basaltic andesite, basaltic trachyandesite, and trachyandesite (Fig. 8), which have relatively high $SiO_2$ contents ranging from 55.1 to 58.5 wt%. They commonly have $Fe_2O_3$ = 5.5–7.4 wt%, $TiO_2$ = 0.8–1.2 wt%, $Al_2O_3$ = 14–18 wt%, MgO = 2.9–3.6 wt% (except sample BB-17-455), and $P_2O_5$ = 0.1–0.4 wt% (Fig. 9). Their Mg# values range between 47.2 and 56.9, except the sample BB-17-455. In addition, all samples from Group 3 display low Zr/Nb ratios (21–28.3) and high $Al_2O_3/TiO_2$ ratios (13.1–22.3) (Table 2). In the MgO vs. major and trace-element plots, these rock samples show narrowed ranges for most elements (e.g., $TiO_2$, $P_2O_5$, La, Sm, and Nb), whereas the contents of $Al_2O_3$ and Th decrease with the increasing MgO content (Fig. 9). The chondrite-normalized REE diagram of Group 3 subvolcanic rocks

**Table 2**
Major (wt%) and trace elements (ppm) of intermediate-mafic rocks from the Tsoroidog Uul' accretionary complex.

| Group | Group 1 | Group 1 | Group 2 | Group 2 | Group 2 | Group 2 | Group 2 | Group 2 |
|---|---|---|---|---|---|---|---|---|
| | 1 | 2 | 3 | 4 | 5 | 6 | 7 | 8 |
| Sample | HH-17-153 | BB-17-444/1 | HH-17-124 | BB-17-341 | HH-26-16 | BB-16-30 | HH-18-35 | HH-17-125/1 |
| $SiO_2$ | 49.17 | 49.06 | 46.59 | 46.00 | 46.89 | 48.77 | 44.85 | 38.36 |
| $TiO_2$ | 1.70 | 1.73 | 3.39 | 2.28 | 1.86 | 2.07 | 3.90 | 4.71 |
| $Al_2O_3$ | 13.30 | 14.47 | 14.53 | 15.29 | 15.09 | 15.57 | 14.71 | 9.88 |
| $Fe_2O_3$ | 12.21 | 10.87 | 10.56 | 9.78 | 9.90 | 11.78 | 13.38 | 20.31 |
| MnO | 0.16 | 0.17 | 0.10 | 0.13 | 0.15 | 0.18 | 0.20 | 0.34 |
| MgO | 6.54 | 5.81 | 4.78 | 9.07 | 7.76 | 5.20 | 7.40 | 9.82 |
| CaO | 8.33 | 9.83 | 7.73 | 7.17 | 8.65 | 6.97 | 6.70 | 8.15 |
| $Na_2O$ | 3.72 | 3.20 | 2.60 | 2.58 | 3.53 | 3.27 | 3.00 | 2.46 |
| $K_2O$ | 0.18 | 0.21 | 3.55 | 1.06 | 0.30 | 0.41 | 1.62 | 0.52 |
| $P_2O_5$ | 0.12 | 0.15 | 1.26 | 0.28 | 0.27 | 0.40 | 0.47 | 0.80 |
| L.O.I. | 3.37 | 3.49 | 3.37 | 5.14 | 5.16 | 5.03 | 4.14 | 3.22 |
| Total | 98.80 | 98.95 | 98.68 | 98.74 | 99.56 | 99.65 | 100.37 | 98.64 |
| Mg# | 54.3 | 54.3 | 50.2 | 67.3 | 63.5 | 49.5 | 55.1 | 51.8 |
| La | 3.80 | 8.10 | 156 | 18.6 | 19.0 | 25.3 | 24.4 | 85.9 |
| Ce | 11.2 | 20.0 | 320 | 39.8 | 40.9 | 53.1 | 56.2 | 172 |
| Pr | 1.65 | 2.63 | 33.6 | 4.61 | 4.35 | 5.75 | 6.64 | 18.6 |
| Nd | 9.40 | 13.0 | 128 | 20.5 | 17.6 | 23.4 | 29.7 | 74.1 |
| Sm | 3.70 | 4.20 | 24.7 | 5.20 | 5.00 | 6.40 | 7.90 | 14.9 |
| Eu | 1.38 | 1.49 | 7.28 | 1.77 | 1.37 | 2.20 | 2.45 | 4.14 |
| Gd | 5.24 | 5.50 | 17.0 | 5.27 | 4.83 | 6.34 | 8.01 | 10.2 |
| Tb | 0.90 | 0.87 | 2.24 | 0.80 | 0.80 | 0.98 | 1.19 | 1.30 |
| Dy | 6.27 | 5.80 | 11.6 | 5.16 | 4.64 | 5.80 | 6.31 | 7.12 |
| Ho | 1.31 | 1.26 | 1.99 | 1.03 | 0.98 | 1.17 | 1.18 | 1.23 |
| Er | 3.95 | 3.52 | 4.97 | 2.97 | 2.82 | 2.97 | 3.12 | 2.98 |
| Tm | 0.59 | 0.54 | 0.65 | 0.44 | 0.38 | 0.45 | 0.42 | 0.36 |
| Yb | 4.00 | 3.40 | 4.10 | 2.9 | 2.60 | 2.80 | 2.80 | 2.50 |
| Lu | 0.68 | 0.59 | 0.58 | 0.44 | 0.73 | 0.05 | 0.37 | 0.38 |
| Sc | 43.0 | 37.0 | 14.0 | 37.0 | 36.0 | 23.0 | 32.0 | 19.0 |
| Co | 42.4 | 40.4 | 23.2 | 37.0 | 43.6 | 38.7 | 41.6 | 73.1 |
| Cs | 0.10 | 0.20 | 2.50 | 1.30 | 0.70 | 0.30 | 0.90 | 0.10 |
| Cr | 120 | 306 | 10.0 | 191 | 386 | 175 | 158 | 243 |
| Hf | 2.00 | 3.00 | 17.0 | 3.00 | 3.00 | 4.00 | 5.00 | 10.0 |
| Ta | 0.50 | 0.60 | 10.1 | 1.70 | 1.30 | 1.00 | 2.00 | 5.40 |
| Th | 0.10 | 0.80 | 15.3 | 1.90 | 3.90 | 3.40 | 2.40 | 8.40 |
| U | 0.05 | 0.12 | 2.91 | 0.42 | 0.52 | 0.68 | 0.60 | 1.55 |
| Ba | 223 | 55.0 | 991 | 183 | 114 | 165 | 496 | 451 |
| Rb | 3.20 | 4.60 | 97.7 | 12.9 | 4.00 | 9.00 | 22.2 | 4.40 |
| Sr | 636 | 162 | 1390 | 480 | 164 | 221 | 282 | 790 |
| Y | 35.4 | 32.1 | 50.5 | 26.5 | 23.7 | 27.6 | 29.9 | 30.8 |
| Zr | 73.8 | 107 | 821 | 144 | 120 | 151 | 226 | 437 |
| Nb | 3.00 | 9.00 | 165 | 27.0 | 17.0 | 19.0 | 31.0 | 88.0 |
| Nb/Y | 0.08 | 0.28 | 3.27 | 1.02 | 0.72 | 0.69 | 1.04 | 2.86 |
| Ba/Rb | 69.7 | 12.0 | 10.2 | 14.2 | 28.5 | 18.3 | 22.3 | 102 |
| Zr/Nb | 24.6 | 12.0 | 4.98 | 5.33 | 7.06 | 7.95 | 7.29 | 4.97 |
| Zr/Hf | 36.9 | 35.7 | 48.3 | 48.0 | 40.0 | 37.8 | 45.2 | 43.7 |
| $Al_2O_3/TiO_2$ | 7.82 | 8.36 | 4.29 | 6.71 | 8.11 | 7.52 | 3.77 | 2.10 |
| Sr/Y | 18.0 | 5.05 | 27.5 | 18.1 | 6.92 | 8.01 | 9.43 | 25.7 |
| (La/Sm)n | 0.66 | 1.25 | 4.08 | 2.31 | 2.45 | 2.55 | 1.99 | 3.72 |
| (Gd/Yb)n | 1.08 | 1.34 | 3.43 | 1.50 | 1.54 | 1.87 | 2.36 | 3.38 |
| (La/Yb)n | 0.68 | 1.71 | 27.3 | 4.60 | 5.24 | 6.48 | 6.25 | 24.7 |
| (Ce/Yb)pm | 0.78 | 1.63 | 21.7 | 3.81 | 4.37 | 5.27 | 5.57 | 19.1 |
| (Nb/La)pm | 0.76 | 1.07 | 1.02 | 1.40 | 0.86 | 0.72 | 1.20 | 0.99 |
| (Th/La)pm | 0.21 | 0.80 | 0.79 | 0.83 | 1.66 | 0.95 | 0.79 | 0.79 |
| (Nb/Th)pm | 3.58 | 1.34 | 1.29 | 1.69 | 0.52 | 0.67 | 1.53 | 1.25 |

| Group | Group 2 | Group 2 | Group 3 | Group 3 | Group 3 | Group 3 | Group 3 |
|---|---|---|---|---|---|---|---|
| Sample | 9 | 10 | 11 | 12 | 13 | 14 | 15 |
| | HH-18-24 | HH-18-17 | HH-17-100/1 | HH-17-143/1 | HH-17-143/2 | BB-17-455 | HH-18-32 |
| SiO2 | 43.50 | 43.32 | 58.50 | 55.70 | 55.96 | 55.05 | 56.37 |
| TiO2 | 2.14 | 2.26 | 1.16 | 0.85 | 0.86 | 0.76 | 0.81 |
| Al2O3 | 12.11 | 13.38 | 15.15 | 16.37 | 16.62 | 13.96 | 18.02 |
| Fe2O3 | 11.85 | 12.10 | 5.48 | 6.99 | 7.08 | 7.43 | 7.10 |
| MnO | 0.22 | 0.15 | 0.07 | 0.18 | 0.15 | 0.13 | 0.16 |
| MgO | 12.25 | 7.00 | 3.25 | 3.60 | 3.53 | 7.47 | 2.85 |
| CaO | 11.28 | 13.37 | 4.13 | 3.79 | 3.91 | 5.35 | 4.46 |
| Na2O | 1.80 | 2.79 | 4.35 | 3.73 | 3.66 | 2.87 | 3.96 |
| K2O | 0.39 | 0.28 | 3.68 | 3.35 | 3.22 | 2.11 | 2.81 |
| P2O5 | 0.64 | 0.55 | 0.43 | 0.19 | 0.18 | 0.14 | 0.22 |
| L.O.I. | 4.08 | 5.17 | 2.76 | 3.79 | 3.24 | 3.32 | 3.17 |
| Total | 100.26 | 100.37 | 99.05 | 98.92 | 98.75 | 98.62 | 99.93 |

**Table 2** (*continued*)

| Group | Group 2 | Group 2 | Group 3 | Group 3 | Group 3 | Group 3 | Group 3 |
|---|---|---|---|---|---|---|---|
| Sample | 9 | 10 | 11 | 12 | 13 | 14 | 15 |
| | HH-18-24 | HH-18-17 | HH-17-100/1 | HH-17-143/1 | HH-17-143/2 | BB-17-455 | HH-18-32 |
| Mg# | 69.7 | 56.3 | 56.9 | 53.4 | 52.6 | 69.1 | 47.2 |
| La | 53.7 | 29.8 | 48.6 | 29.0 | 27.5 | 20.6 | 34.5 |
| Ce | 103 | 63.2 | 99.1 | 59.4 | 55.7 | 40.6 | 69.4 |
| Pr | 10.4 | 7.41 | 10.4 | 6.26 | 5.93 | 4.56 | 7.31 |
| Nd | 41.6 | 30.9 | 39.2 | 24.4 | 23.5 | 18.9 | 27.3 |
| Sm | 8.60 | 7.20 | 7.50 | 5.50 | 5.20 | 4.30 | 5.60 |
| Eu | 2.47 | 2.03 | 1.85 | 1.94 | 1.92 | 1.16 | 3.11 |
| Gd | 8.70 | 7.14 | 4.37 | 4.40 | 4.35 | 3.72 | 5.52 |
| Tb | 1.17 | 1.03 | 0.54 | 0.71 | 0.66 | 0.58 | 0.83 |
| Dy | 5.39 | 4.98 | 2.82 | 4.02 | 3.95 | 3.28 | 3.92 |
| Ho | 1.00 | 0.91 | 0.45 | 0.83 | 0.78 | 0.71 | 0.80 |
| Er | 2.57 | 2.35 | 1.33 | 2.51 | 2.32 | 1.88 | 2.34 |
| Tm | 0.31 | 0.31 | 0.15 | 0.34 | 0.30 | 0.27 | 0.30 |
| Yb | 2.40 | 2.00 | 1.10 | 2.40 | 2.40 | 2.10 | 2.30 |
| Lu | 0.30 | 0.27 | 0.14 | 1.86 | 0.38 | 0.35 | 0.34 |
| Sc | 43.0 | 296 | 10.0 | 17.0 | 18.0 | 22.0 | 15.0 |
| Co | 55.8 | 43.9 | 17.3 | 21.1 | 20.1 | 31.9 | 17.3 |
| Cs | 0.30 | 0.30 | 0.70 | 3.40 | 3.60 | 1.00 | 1.10 |
| Cr | 561 | 305 | 78.0 | 134 | 41.0 | 571 | 42.0 |
| Hf | 5.00 | 4.00 | 5.00 | 4.00 | 4.00 | 3.00 | 5.00 |
| Ta | 3.70 | 1.90 | 0.50 | 0.50 | 0.50 | 0.50 | 0.50 |
| Th | 6.60 | 3.10 | 8.40 | 5.70 | 5.70 | 3.70 | 8.30 |
| U | 1.51 | 1.06 | 1.96 | 1.63 | 1.52 | 0.95 | 1.81 |
| Ba | 301 | 119 | 1093 | 2939 | 3162 | 624 | 2396 |
| Rb | 8.10 | 7.20 | 78.1 | 81.0 | 82.8 | 52.5 | 51.8 |
| Sr | 260 | 296 | 753 | 535 | 555 | 496 | 1236 |
| Y | 24.0 | 22.4 | 12.8 | 21.7 | 22.9 | 18.6 | 21.4 |
| Zr | 202 | 174 | 245 | 168 | 169 | 105 | 198 |
| Nb | 67.0 | 34.0 | 10.0 | 7.00 | 7.00 | 5.00 | 7.00 |
| Nb/Y | 2.79 | 1.52 | 0.78 | 0.32 | 0.31 | 0.27 | 0.30 |
| Ba/Rb | 37.2 | 16.5 | 14.0 | 36.3 | 38.2 | 11.9 | 46.3 |
| Zr/Nb | 3.01 | 5.12 | 24.5 | 24.0 | 24.1 | 21.0 | 28.3 |
| Zr/Hf | 40.4 | 43.5 | 49.0 | 42.0 | 42.3 | 35.0 | 39.6 |
| $Al_2O_3/TiO_2$ | 5.66 | 5.92 | 13.1 | 19.3 | 19.3 | 18.4 | 22.3 |
| Sr/Y | 10.8 | 13.2 | 58.8 | 24.7 | 24.2 | 26.7 | 57.8 |
| (La/Sm)n | 4.03 | 2.67 | 4.18 | 3.40 | 3.41 | 3.09 | 4.00 |
| (Gd/Yb)n | 2.99 | 2.95 | 3.30 | 1.50 | 1.50 | 1.50 | 2.00 |
| (La/Yb)n | 16.0 | 10.7 | 31.7 | 8.67 | 8.22 | 7.04 | 10.8 |
| (Ce/Yb)pm | 11.9 | 8.78 | 25.0 | 6.87 | 6.45 | 5.37 | 8.40 |
| (Nb/La)pm | 1.20 | 1.09 | 0.20 | 0.23 | 0.25 | 0.23 | 0.20 |
| (Th/La)pm | 0.99 | 0.84 | 1.40 | 1.59 | 1.68 | 1.45 | 1.90 |
| (Nb/Th)pm | 1.21 | 1.31 | 0.14 | 0.15 | 0.15 | 0.16 | 0.10 |

| Group | Group 4 | Group 4 | Group 4 | Group 4 | Group 4 | Group 4 | Group 4 |
|---|---|---|---|---|---|---|---|
| Sample | 16 | 17 | 18 | 19 | 20 | 21 | 22 |
| | HH-17-151 | HH-18-26 | HH-141-16 | HH-65-16 | BB-16-11 | HH-121-16 | HH-57-16 |
| $SiO_2$ | 49.95 | 47.23 | 49.43 | 47.94 | 49.92 | 48.83 | 46.94 |
| $TiO_2$ | 1.19 | 1.48 | 1.17 | 2.11 | 1.76 | 1.55 | 0.97 |
| $Al_2O_3$ | 13.89 | 15.23 | 14.04 | 13.03 | 13.29 | 13.51 | 15.17 |
| $Fe_2O_3$ | 10.25 | 11.49 | 10.88 | 13.72 | 13.24 | 11.61 | 10.40 |
| MnO | 0.14 | 0.27 | 0.20 | 0.22 | 0.21 | 0.19 | 0.19 |
| MgO | 8.06 | 9.18 | 7.08 | 6.04 | 6.14 | 7.71 | 7.14 |
| CaO | 6.99 | 8.10 | 9.95 | 8.23 | 7.98 | 9.24 | 8.86 |
| $Na_2O$ | 4.01 | 2.16 | 2.37 | 2.72 | 2.75 | 3.20 | 2.21 |
| $K_2O$ | 0.63 | 0.37 | 0.70 | 0.41 | 1.22 | 0.32 | 2.29 |
| $P_2O_5$ | 0.06 | 0.12 | 0.09 | 0.17 | 0.16 | 0.13 | 0.07 |
| L.O.I. | 3.43 | 4.62 | 3.01 | 5.18 | 3.01 | 3.25 | 5.09 |
| Total | 98.60 | 100.25 | 98.92 | 99.77 | 99.68 | 99.54 | 99.33 |
| Mg# | 63.6 | 64.0 | 59.1 | 49.5 | 50.8 | 59.6 | 60.4 |
| La | 2.30 | 3.40 | 3.10 | 6.40 | 5.70 | 5.50 | 3.80 |
| Ce | 7.00 | 10.0 | 8.30 | 17.5 | 15.3 | 16.2 | 8.90 |
| Pr | 1.06 | 1.56 | 1.27 | 2.41 | 1.92 | 2.03 | 1.19 |
| Nd | 6.30 | 9.10 | 6.70 | 12.5 | 9.90 | 9.20 | 7.30 |
| Sm | 2.60 | 3.60 | 3.00 | 5.00 | 3.70 | 3.30 | 2.20 |
| Eu | 0.93 | 1.20 | 1.08 | 1.68 | 1.31 | 1.19 | 0.96 |
| Gd | 3.63 | 4.56 | 4.04 | 6.64 | 4.85 | 4.01 | 2.93 |
| Tb | 0.66 | 0.82 | 0.73 | 1.17 | 0.89 | 0.69 | 0.51 |
| Dy | 4.53 | 5.41 | 4.90 | 7.72 | 5.85 | 4.26 | 3.50 |
| Ho | 0.98 | 1.13 | 1.13 | 1.79 | 1.33 | 0.93 | 0.84 |

(*continued on next page*)

**Table 2** (*continued*)

| Group | Group 4 | Group 4 | Group 4 | Group 4 | Group 4 | Group 4 | Group 4 |
|---|---|---|---|---|---|---|---|
| Sample | 16 | 17 | 18 | 19 | 20 | 21 | 22 |
| | HH-17-151 | HH-18-26 | HH-141-16 | HH-65-16 | BB-16-11 | HH-121-16 | HH-57-16 |
| Er | 3.07 | 3.42 | 3.29 | 4.95 | 3.92 | 2.62 | 2.31 |
| Tm | 0.43 | 0.48 | 0.50 | 0.79 | 0.59 | 0.38 | 0.36 |
| Yb | 2.90 | 3.40 | 3.40 | 5.20 | 4.00 | 2.60 | 2.30 |
| Lu | 0.47 | 0.46 | 0.20 | 0.72 | 0.20 | 0.47 | 0.05 |
| Sc | 38.0 | 44.0 | 40.0 | 49.0 | 43.0 | 38.0 | 41.0 |
| Co | 40.4 | 43.4 | 45.5 | 42.2 | 36.0 | 36.2 | 47.0 |
| Cs | 0.30 | 0.20 | 0.50 | 0.40 | 0.80 | 0.30 | 1.10 |
| Cr | 25.6 | 29.4 | 28.1 | 39.8 | 31.4 | 22.9 | 18.3 |
| Hf | 2.00 | 2.00 | 2.00 | 4.00 | 3.00 | 3.00 | 2.00 |
| Ta | 0.50 | 0.50 | 0.50 | 0.50 | 0.50 | 0.50 | 0.50 |
| Th | 0.60 | 0.30 | 0.70 | 2.00 | 1.00 | 1.50 | 2.90 |
| U | 0.05 | 0.09 | 0.07 | 0.94 | 0.13 | 0.14 | 0.10 |
| Ba | 176 | 54.0 | 84.0 | 242 | 157 | 97.1 | 542 |
| Rb | 16.9 | 7.40 | 21.4 | 9.50 | 14.0 | 4.70 | 50.6 |
| Sr | 104 | 116 | 263 | 98.7 | 77.7 | 136 | 250 |
| Y | 25.6 | 29.4 | 28.1 | 39.8 | 31.4 | 22.9 | 18.3 |
| Zr | 40.7 | 78.3 | 59.8 | 112 | 87.2 | 89.0 | 46.2 |
| Nb | 2.00 | 2.00 | 1.00 | 3.00 | 4.00 | 3.00 | 2.00 |
| Nb/Y | 0.08 | 0.07 | 0.04 | 0.08 | 0.13 | 0.13 | 0.11 |
| Ba/Rb | 10.4 | 7.30 | 3.93 | 25.5 | 11.2 | 20.66 | 10.7 |
| Zr/Nb | 20.4 | 39.2 | 59.8 | 37.3 | 21.8 | 29.7 | 23.1 |
| Zr/Hf | 20.4 | 39.2 | 29.9 | 28.0 | 29.1 | 29.7 | 23.1 |
| $Al_2O_3/TiO_2$ | 11.7 | 10.3 | 12.0 | 6.18 | 7.55 | 8.72 | 15.6 |
| Sr/Y | 4.06 | 3.95 | 9.36 | 2.48 | 2.47 | 5.94 | 13.7 |
| (La/Sm)n | 0.57 | 0.60 | 0.67 | 0.83 | 0.99 | 1.08 | 1.12 |
| (Gd/Yb)n | 1.04 | 1.10 | 0.98 | 1.06 | 1.00 | 1.28 | 1.05 |
| (La/Yb)n | 0.57 | 0.71 | 0.65 | 0.88 | 1.02 | 1.52 | 1.19 |
| (Ce/Yb)pm | 0.67 | 0.82 | 0.68 | 0.93 | 1.06 | 1.73 | 1.07 |
| (Nb/La)pm | 0.84 | 0.56 | 0.31 | 0.45 | 0.68 | 0.53 | 0.51 |
| (Th/La)pm | 2.11 | 0.71 | 1.34 | 1.38 | 1.13 | 2.13 | 1.03 |
| (Nb/Th)pm | 0.40 | 0.79 | 0.17 | 0.18 | 0.48 | 0.24 | 0.08 |

Note: Columns: 1–2 – Group 1 (MORB); 3–10 – Group 2 (OIB); 11–15 – Group 3 (calc-alkaline basalt); 16–22 – Group 4 (VAT).

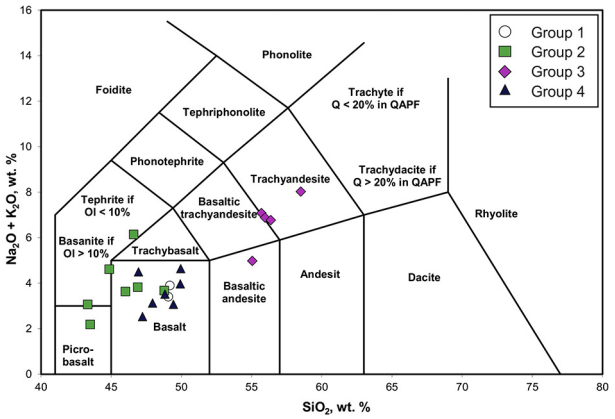


**Fig. 8.** Silica vs. alkalis diagram (TAS; Le Maitre 2002) for the intermediate-mafic rocks from the Tsoroidog Uul' accretionary complex.

have patterns regularly decreasing from LREE to HREE with $La/Yb_n$ ratio (7–31.7), $La/Sm_n$ ratio (3.1–4.2), and $Gd/Yb_n$ ratio (1.5–3.3) (Fig. 10f). The primitive mantle-normalized multi-element patterns of these rock samples show negative Nb ($Nb/La_{pm}$ = 0.2–0.3; $Nb/Th_{pm}$ = 0.1–0.2) and Ti anomalies (Fig. 10e), whereas significant enrichment of LILE (K, Rb, Ba, Sr) is noticeable compared with the other groups of rocks (Table 2).

Group 4 consists of basalts with a sub-alkaline or tholeiitic affinity (Fig. 8). These basaltic rocks display low Nb/Y ratio (<0.1, Table 2) and variable contents of $SiO_2$ (46.9–50.0 wt%), $Fe_2O_3$ (10.3–13.7 wt%), $TiO_2$ (1.0–2.1 wt%), $Al_2O_3$ (13.0–15.2 wt%), MgO (6.0–9.2 wt%), $P_2O_5$ (0.1–0.2 wt%), and Mg# values (49.5–63.6). Except sample HH-141-16, all the rock samples are characterized by high Zr/Nb ratio (20.4–39.2) which is higher than those of other groups. Their $Al_2O_3/TiO_2$ ratios range from 6.2 to 15.6 (Table 2).The $TiO_2$, $Fe_2O_3$ and La contents are negatively correlated with MgO and decrease with increasing MgO, whereas $Al_2O_3$ is positively correlated with MgO, and $P_2O_5$,Th, Nb and Sm contents are relatively constant with increasing MgO content (Fig. 9).The chondrite-normalized REE diagrams of these basaltic rock samples display relatively flat patterns($La/Yb_n$ = 0.6–1.5)and show slight depletion in LREE ($La/Sm_n$ = 0.6–1.1) with respect to HREE ($Gd/Yb_n$ = 1.0–1.3) (Fig. 10h). On the primitive mantle-normalized multi-element diagram, they possess obvious Th enrchiment ($Nb/Th_{pm}$ = 0.1–0.8), Nb depletion ($Nb/La_{pm}$ = 0.3–0.8), and no negative Ti anomalies (Fig. 10g).

### 4.3. Whole-rock Sm—Nd isotopes

The whole-rock Sm—Nd isotopic data of the intermediate-mafic rocks are listed in Table 3. The initial isotopic ratios were recalculated according to the Lower Devonian age based on the Sm—Nd dating of basaltic tufficeous rock from the Erdenetsogt Formation surrounding the Uyanga area in the Tsetserleg terrane (Orolmaa and Erdenesaikhan, 2008). The moderate-Ti samples (geochemically close to MORB) and the high-Ti samples (geochemically close to OIB) were recalculated at ~400 Ma. The low-Ti samples (geochemically close to CAB) were recalculated at ~300 Ma because we assume that these rocks probably crystallized after the TUAC formed during the Early Carboniferous (see Section 2.2). Overall,

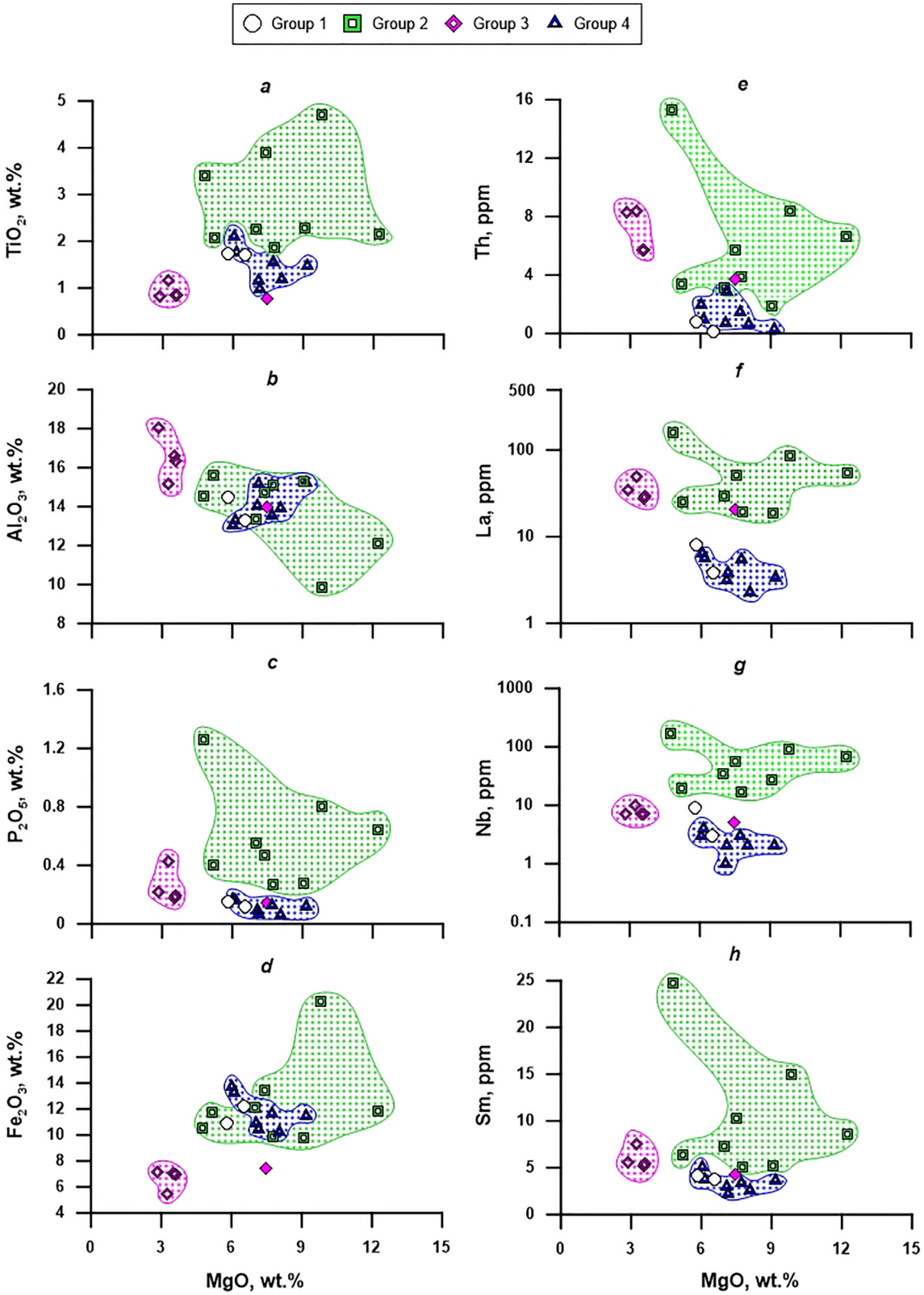


**Fig. 9.** Binary diagrams of MgO vs. (a) ($TiO_2$), (b) $Al_2O_3$, (c) $P_2O_5$, (d) $Fe_2O_3$, (e) Th, (f) La, (g) Nb and (h) Sm for the intermediate-mafic rocks from the Tsoroidog Uul' accretionary complex.

these samples have both positive and negative εNd(t) values. The samples geochemical similar to MORB and OIB have higher $^{143}Nd/^{144}Nd$ ratios (0.5129–05131), whereas the samples geochemical similar to CAB have lower $^{143}Nd/^{144}Nd$ ratios (0.5119) (Table 3). The samples from Group 1 and Group 2 which contain moderate- and high-Ti contents have positive εNd(t) values ranging from +7.8 to +8.2. In contrast, the sample from Group 3 which has low-Ti compositions show negative εNd(t) value (−12.0) (Table 3).

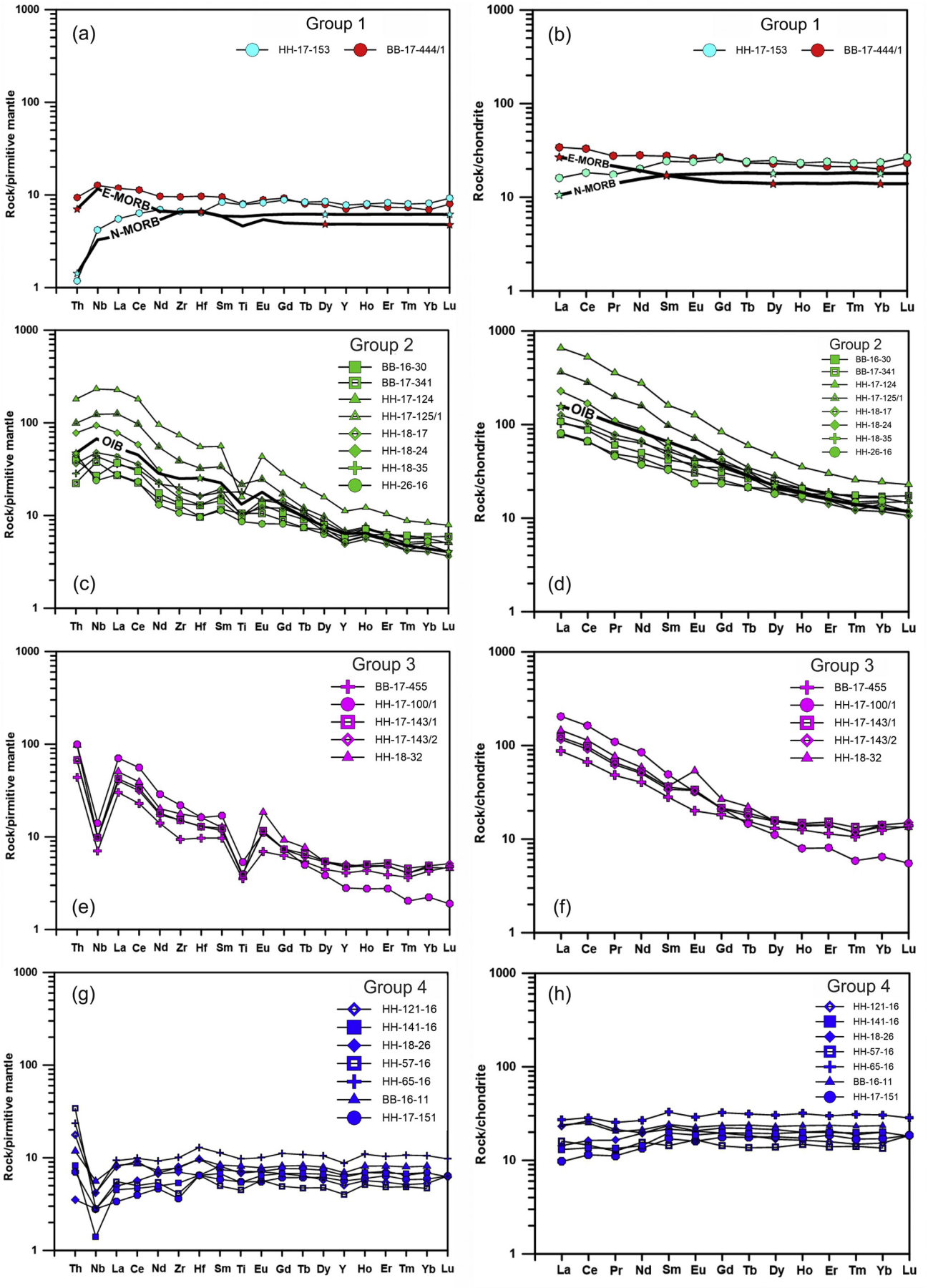
(a)
Group 1
HH-17-153
BB-17-444/1
E-MORB
N-MORB
Rock/pirmitive mantle
Th Nb La Ce Nd Zr Hf Sm Ti Eu Gd Tb Dy Y Ho Er Tm Yb Lu
(b)
Group 1
HH-17-153
BB-17-444/1
E-MORB
N-MORB
Rock/chondrite
La Ce Pr Nd Sm Eu Gd Tb Dy Ho Er Tm Yb Lu
(c)
Group 2
BB-16-30
BB-17-341
HH-17-124
HH-17-125/1
HH-18-17
HH-18-24
HH-18-35
HH-26-16
OIB
Rock/pirmitive mantle
(d)
Group 2
BB-16-30
BB-17-341
HH-17-124
HH-17-125/1
HH-18-17
HH-18-24
HH-18-35
HH-26-16
OIB
Rock/chondrite
(e)
Group 3
BB-17-455
HH-17-100/1
HH-17-143/1
HH-17-143/2
HH-18-32
Rock/pirmitive mantle
(f)
Group 3
BB-17-455
HH-17-100/1
HH-17-143/1
HH-17-143/2
HH-18-32
Rock/chondrite
(g)
Group 4
HH-121-16
HH-141-16
HH-18-26
HH-57-16
HH-65-16
BB-16-11
HH-17-151
Rock/pirmitive mantle
(h)
Group 4
HH-121-16
HH-141-16
HH-18-26
HH-57-16
HH-65-16
BB-16-11
HH-17-151
Rock/chondrite

**Table 3**
Whole rock Sm—Nd isotope data of intermediate-mafic rocks from the Tsoroidog Uul' accretionary complex.

| Sample | BB-17-444/1 | HH-17-124 | HH-17-100/1 |
|---|---|---|---|
| Group | Group 1 | Group 2 | Group 3 |
| Age, Ma | 400 | 400 | 300 |
| Sm, ppm | 4.9 | 16.47 | 7.19 |
| Nd, ppm | 14.49 | 71.03 | 38.56 |
| $^{147}Sm/^{144}Nd$ | 0.20434 | 0.14017 | 0.1127 |
| $^{143}Nd/^{144}Nd$ | 0.513078 | 0.512888 | 0.511858 |
| $\varepsilon_{Nd}(0)$ | 8.6 | 4.9 | −15.2 |
| $\varepsilon_{Nd}(T)$ | 8.2 | 7.8 | −12 |
| $T_{Nd}(DM)$ | 1206 | 547 | 1948 |
| $T_{Nd}(DM\text{-}2st)$ | 480 | 516 | 2068 |

Note: No precise age data was reported for these three groups of rocks, and the age listed in this table was estimated based on geological relationship between different units and might not be precise.

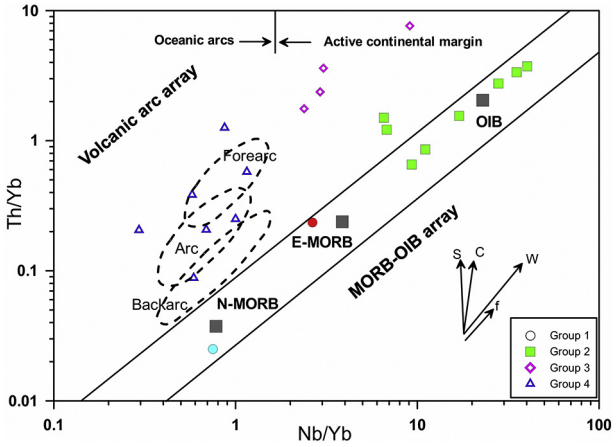


**Fig. 11.** Th/Yb vs. Nb/Yb plot for the intermediate-mafic rocks from the Tsoroidog Uul' accretionary complex (after Pearce 2008). N-MORB: normal mid-ocean ridge basalt, E-MORB: enriched mid-ocean ridge basalt, OIB: oceanic island basalt.

## 5. Discussion

### 5.1. Petrogenesis and mantle sources

Overall, the TUAC incorporates a wide range of intermediate-mafic rock types as shown in the previous sections. The geochemical characteristics of these rocks can be used for determining the nature and petrogenesis of the magmatic events which occurred in the Tsetserleg terrane from the Khangay-Khentey orogenic system. In this study, we discuss the petrogenesis of volcanic and subvolcanic rocks based on the less mobile incompatible elements and stable isotopic values of these rocks. Some elements (e.g., Zr, $TiO_2$, Y, Sc, Ce, and Nb) are largely immobile during the alteration of volcanic rocks owing to metamorphism, hydrothermal events and weathering (Floyd and Winchester, 1975). Hence, we mainly selected these elements for petrogenetic interpretation (Figs. 11 and 12).

Constraining the mantle source characteristics is important when considering the petrogenesis of mafic and basaltic rocks (Li et al., 2013, 2016; Liu et al., 2020; Sun et al., 2019; Wang et al., 2019; Wu et al., 2017a). The Zr vs. Nb discrimination diagram (Fig. 13a, b) indicates that Group 2 basaltic rocks were generated from an enriched-type mantle source, whereas other rock groups were originated from depleted-type mantle sources. Group 1 (MORB) and Group 2 (OIB) basaltic rocks plot along the MORB-OIB array, whereas Group 3 (calc-alkaline) and Group 4 (volcanic arc tholeiite) basaltic rocks plot along the volcanic arc array in the $Th_N$ vs. $Nb_N$ discrimination diagram (Fig. 12a). Moreover, Group 2 rocks contain moderate to high Ti contents and have a positive εNd(t) value (+7.8), indicating a enriched mantle source. In contrast, Group 3 rocks have low Ti compositions and display negative εNd(t) value (−12.0). This suggests that these rocks were derived from a mantle source with crustal materials input (Safonova et al., 2020).

Some trace element contents (e.g., Nb, Th, and REE) and trace element ratios (e.g., Nb/Yb, Th/Ta, Th/Nb, and Ba/Th) are moderately affected by fractional crystallization of predominantly olivine + clinopyroxene + plagioclase (Saccani et al., 2018). Therefore, we use the melting model of Nb/Yb vs. Th (Fig. 14) for estimating the composition of mantle source and the degree of partial melting for Group 1 and Group 2 rocks. However, this diagram is not entirely suitable for modelling the possible mantle sources for Group 3 and Group 4 rocks. Hence, we use the Cr vs. Y diagram (Fig. 15) for estimating the composition of mantle source and the degree of partial melting for these volcanic and subvolcanic rocks. These two plots further support that Group 1, Group 2, Group 3 and Group 4 rocks have typical features of MORB, OIB, calc-alkaline and volcanic arc tholeiite, respectively. We discuss the mantle source for each group of rocks in detail in the following paragraphs.

Group 1 basalts have geochemical characteristics indicating melt originated from a depleted mantle source in a mid-oceanic ridge setting. MORB-type basalts were formed during the decompressional melting of upper mantle material at the mid-oceanic ridge and compose a large part of Ocean Plate Stratigraphy (OPS) (Isozaki, 1997). In general, OPS is characterized by regular lithologic facies change of basalt through pelagic to hemipelagic depositional succession, and the units are incorporated into accretionary complexes (terrigenous rocks) during the subduction of the oceanic plate (Isozaki, 1997; Safonova et al., 2016). In contrast, accretionary complexes typically consist of igneous and sedimentary rocks scraped from the subducting oceanic plate, including basalt, chert, mudstone, siltstone, shale and sandstone (Safonova et al., 2020). Moreover, normal mid-oceanic ridge basalts (N-MORB) are more depleted of incompatible elements than enriched mid-oceanic ridge basalts (*E*-MORB) and oceanic island basalts (OIB) (Sun and McDonough, 1989). In this study, Group 1 basalts have moderate Ti content and positive εNd(t) = +8.2. However, these basalts can be divided into two subgroups.

The first subgroup has typical Nb = 3.0 ppm, Th = 0.1 ppm, Zr/Nb = 24.6, $La/Sm_n$ = 0.7 and $Ce/Yb_{pm}$ = 0.8, suggesting a depleted MORB mantle (DMM) source for the parent magma. In addition, the $Gd/Yb_n$ = 1.1 (Table 2; Fig. 10b) implies that partial melting occurred in the spinel-facies mantle. The primitive mantle-normalized multi-element pattern reveals a negative Th anomaly relative to Nb ($Nb/Th_{pm}$ = 3.6) (Fig. 10a). The REE and multi-element patterns (Figs. 10a, b) and incompatible trace element plots (Figs. 11 and 12) confirm that the rock was derived from N-MORB-type mantle source without involvement of subduction-related process. The Th vs. Nb/Yb plot (Fig. 14) shows that the composition of this rock is consistent with ~15% of partial melting in the spinel stability field. The model of the Cr vs. Y plot further indicates that the composition of this basalt is compatible with the primary melts generated from ~18% of partial melting of a DMM source (Fig. 15).

The second subgroup has slightly enriched geochemical characteristics than the first subgroup, with typical element contents and ratios of Nb = 9.0 ppm, Th = 0.8 ppm, Zr/Nb = 11.9, $La/Sm_n$ = 1.3, and

**Fig. 10.** Chondrite-normalized rare earth element and primitive mantle-normalized multi-component trace element patterns for (a, b) Group 1 (N-MORB and *E*-MORB), (c, d) Group 2 (OIB), (e, f) Group 3 (calc-alkaline dike), and (g, h) Group 4 (VAT). The normalizing values are from Sun and McDonough (1989).

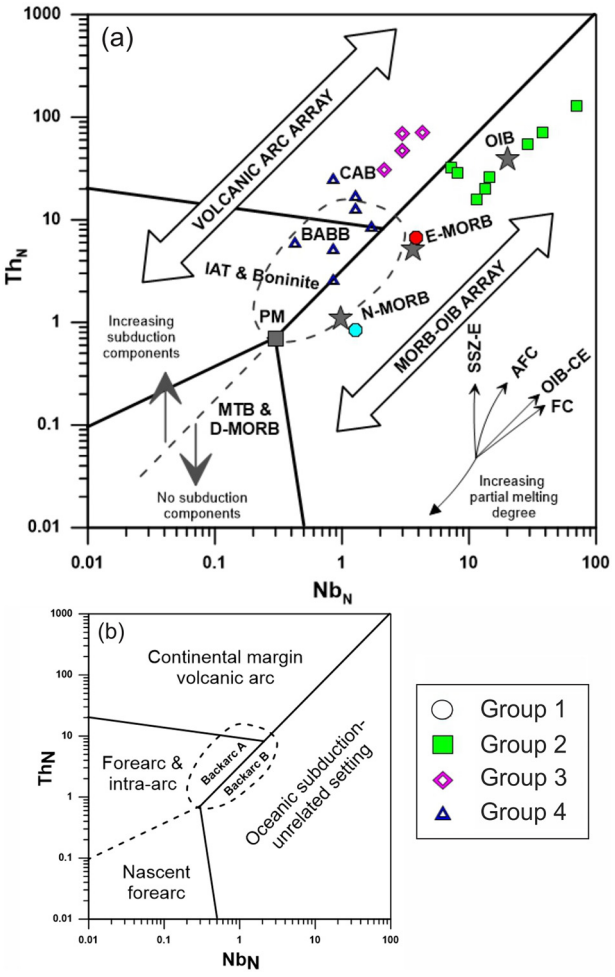


**Fig. 12.** N-MORB-normalized Th vs. Nb discrimination diagram for the intermediate-mafic rocks from the Tsoroidog Uul' accretionary complex (after Saccani et al., 2015): (a) rock-type discrimination, (b) tectonic setting interpretation. MORB: mid-ocean ridge basalt, N-: normal type, E-: enriched type, D-: depleted type, MTB: medium-Ti basalts, IAT: island arc tholeiite, CAB: calc-alkaline basalt; OIB: alkaline oceanic within-plate basalt, BABB: back-arc basin basalt, SSZ-E: supra-subduction zone enrichment, AFC: assimilation fractional crystallization, OIB-CE: OIB component enrichment, FC: fractional crystallization, back-arc A: relatively immature back-arc setting, back-arc B: relatively mature back-arc setting.

$Ce/Yb_{pm} = 1.6$. The flat REE pattern is very similar to those of enriched mid-oceanic ridge basalts (E-MORB) (Sun and McDonough, 1989). The higher concentrations of Nb, Th, and LREE in this subgroup relative to N-MORB suggest that the possible magma source of this rock is likely a sub-oceanic slightly enriched mantle compared to the DMM source (Herzberg, 2004). In the Th/Yb vs. Nb/Yb (Fig. 11) and $Th_N$ vs. $Nb_N$ discrimination diagrams (Fig. 12a), this basalt plots within or near the E-MORB field. Furthermore, the $Gd/Yb_n$ ratio of 1.3 in this rock (Table 2, Fig. 10b) reflects that partial melting occurred in the spinel-facies mantle. The Th vs. Nb/Yb plot (Fig. 14) suggests that the composition of this basalt is consistent with ~17% of partial melting from a spinel-facies OIB source. Nonetheless, this basalt is probably derived from an E-DMM source considering its abovementioned geochemical features (Workman and Hart, 2005).

Group 2 basaltic rocks are characterized by high $TiO_2$, $Nb_{av.} =$ 56 ppm, $Th_{av.} = 5.6$ ppm, $Zr/Nb_{av.} = 5.7$, $La/Sm_{n(av.)} = 3.0$ and $Gd/Yb_{pm(av.)} = 2.5$ (Table 2), as well as high LREE and differentiated HREE patterns (Fig. 10d). These features suggest an oceanic island basalt (OIB) affinity of these basalts (Safonova et al., 2012; Sun and McDonough, 1989). Tholeiitic to alkaline intraplate basalts of oceanic islands (OIB-type) form due to the activity of mantle plumes rising from the core-mantle boundary (Maruyama et al., 2007). They are enriched in incompatible elements such as LREE, Ti, Nb, Rb, K, Cs, Ba and Th (Weaver, 1991). In addition, the high MREE/HREE ratios of Group 2 basaltic rocks (Fig. 10d) imply an involvement of a garnet peridotite source. The MgO contents of these basalts decrease with increasing $SiO_2$, indicating that mafic minerals were removed during magmatic evolution. Moreover, the wide range of geochemical compositions of these rocks probably reflects different degree of fractionation. Olivine and clinopyroxene are the main fractionated minerals in the Group 2 basaltic rocks, and the clinopyroxene-dominated fractionation is shown by the negative correlation between $Al_2O_3$ and MgO (Fig. 9c), suggesting the fractionation of clinopyroxene during early crystallization. The enrichment of most incompatible elements such as Nb, Th, and LREE and positive $\varepsilon Nd(t)$ of +7.8 in Group 2 basalts suggest that the mantle source of these rocks is enriched (Safonova et al., 2011a; Safonova et al., 2020), similar to that of the Emperor-Hawaii volcanoes chain (Regelous et al., 2003). In addition, on the discrimination diagrams (Figs. 11 and 12), Group 2 basalts plot in the OIB fields. Thus, we propose that these basalts were generated from an enriched OIB-type mantle source at the garnet facies ($Gd/Yb_{pm} > 2$) and spinel facies ($Gd/Yb_{pm} < 2$) mantle depths. The Th vs. Nb/Yb plot (Fig. 14) displays that the composition of Group 2 basaltic rocks is compatible with 2.5–5% of partial melting in the spinel stability field and 0.1–10% of partial melting in the garnet stability field. The degree of melting was lower for samples HH-17-124 and HH-17-125/1 so that the melts contained higher concentrations of incompatible elements (Table 2; Safonova et al., 2011a).

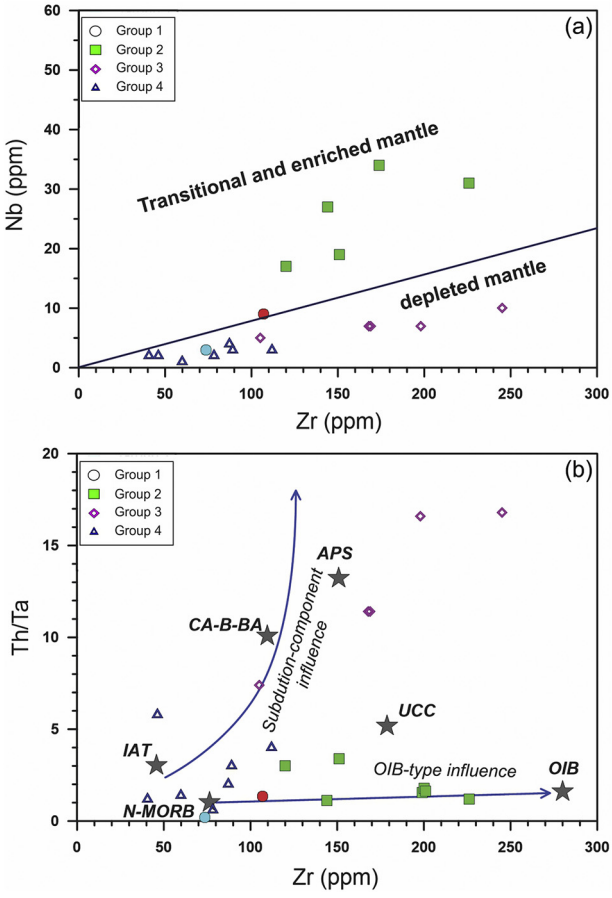


**Fig. 13.** (a) Nb vs. Zr and (b) Th/Ta vs. Zr diagrams for the intermediate-mafic rocks from the Tsoroidog Uul' accretionary complex (after Saccani et al., 2018). Stars indicate the composition of average pelitic sediments (APS), upper continental crust (UCC), average calc-alkaline basalts and basaltic andesites (CA-B-BA), average island arc tholeiitic basalts (IAT), normal-type mid-ocean ridge basalt (N-MORB), and alkaline ocean island basalt (OIB).

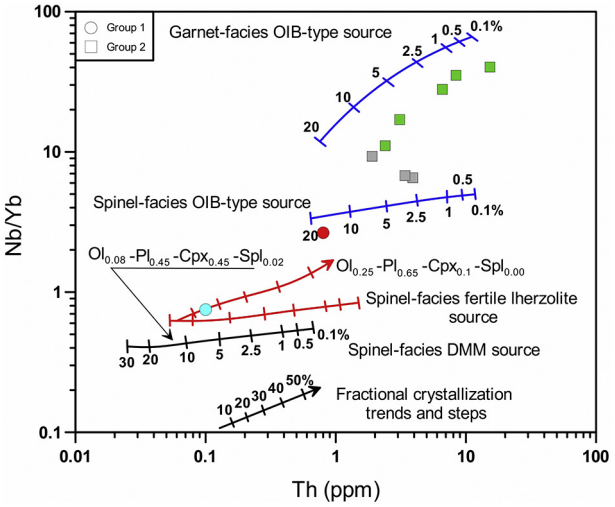


**Fig. 14.** Nb/Yb vs. Th diagram for the mafic rocks from the Tsoroidog Uul' accretionary complex (after Saccani et al., 2018).

Group 3 intermediate rocks are characterized by low $TiO_2$ contents (<1 wt%), high Zr/Nb ratios (average 24.4), $Nb_{av.}$ = 7.2 ppm, $Th_{av.}$ = 6.4 ppm, $La/Sm_{n(av.)}$ = 3.6, and εNd(t) = −12.0. They have high $Th/Nb_N$ ratios (Fig. 12) and are significantly enriched in LREE (Fig. 10f). These geochemical characteristics are consistent with their calc-alkaline affinity (Safonova et al., 2016). The high MgO of sample BB-17-455 implies that the magma might be derived near the volcanic front at mantle depths close to the mantle-crust boundary (Tatsumi, 1982). The high LILE contents of these rock samples compared to those of the MORB (Table 2) obviously indicate a subduction-related process. Depletion of Nb relative to Th and La implies that the source of magma was contaminated by continental materials (Kelemen et al., 1993). In addition, their Th and LREE enrichment indicate that the mantle source was significantly metasomatized by subduction-related components (Saccani et al., 2018). Moreover, the negative Ti anomalies shown in the multi-element patterns (Fig. 10e) are typical geochemical signature of the subduction-related magmatic rocks. The Group 3 intermediate rocks further plot in the field of CAB (calc-alkaline basalts) (Figs. 11 and 12), indicating an arc-related affiliation. The Cr vs. Y plot displays that these rocks might be generated by ~17% partial melting from a depleted mantle source residual after 15% MORB-type melt extraction (Fig. 15). We suggest that the intermediate rocks were probably derived from a mixed source including accretionary sediments and the partial melting products from subducted oceanic slab.

Group 4 basalts are characterized by moderate $TiO_2$, high Zr/Nb ratio (average = 33), $Nb_{av.}$ = 2.4 ppm, $Th_{av.}$ = 1.3 ppm, $La/Sm_{n(av.)}$ = 0.8, and rather flat REE patterns. They are depleted in Ta, Nb, and HFSE (Table 2), which are consistent with an origin from partial melting of refractory mantle sources. In addition, the Cr—Y model (Fig. 15) indicates that most of Group 4 basalts were derived by about 10% partial melting from a depleted mantle source residual after 15% MORB-type melt extraction. Furthermore, the low fractionation of HREE relative to MREE observed in Group 4 basalts (Fig. 10h) and the $Gd/Yb_{pm(av.)}$ = 1.1 suggest that partial melting occurred in the spinel-facies mantle depth. Therefore, we suggest that they were generated from a refractory mantle source, and the primitive magma producing these rocks originated at shallow depths of the mantle.

### 5.2. Tectonic implications for the intermediate-mafic rocks

The geochemical (major and trace element) and isotopic compositions of the volcanic and subvolcanic rocks from the TUAC suggest different tectonic settings (Figs. 16a–e).

Group 1 basalts are compatible with a genesis from primary magma originated from depleted MORB-type and sub-oceanic mantle sources, which are slightly enriched compared to N-MORB source,with no attribute of enriched OIB-type material or subduction-related chemical components (Figs. 10a, b). Thus, we infer that Group 1 samples with moderate Ti contents formed in a mid-oceanic ridge tectonic setting, and represent typical normal mid-oceanic ridge basalt (N-MORB) and enriched mid-oceanic ridge basalt (*E*-MORB), presenting the base of Ocean Plate Stratigraphy.

Group 2 basaltic rocks are consistent with a genesis from primary magmas originated from enriched oceanic mantle source (Figs. 10c, d) with characteristics of enriched incompatible elements. These rocks have high Ti contents and were identified with a biohermian carbonate cup and hemigenous limestonelayers. This suggests an eruption at oceanic islands of the Paleo-Pacific Ocean, similar to those of the Emperor-Hawaii seamounts and volcanoes chain (Fig. 16b). They are probably related to the Pacific hot spot or mantle plume since Middle Paleozoic intraplate basalts of the Ulaanbaatar terrane were suggested to be derived from the Paleo-Asian Ocean plume-related magmatism (Regelous et al., 2003; Safonova et al., 2009; Safonova and Santosh, 2014).

The geochemical features of the studied basalts allow us to recognize two types of source in the mantle depth for OIB-type basalts of the TUAC, and it probably represents two different oceanic islands formed over the Paleo-Pacific Oceanic lithosphere at different ages. Volcanic and subvolcanic rocks from Group 3 and Group 4 display variable ranges of Th enrichment relative to Nb (Fig. 10e, g), suggesting subduction-derived components (Fig. 12a). This is supported by the Th/Ta ratios and Zr compositions (Fig. 13b). In particular, the influence of a subduction component is moderate for Group 4 volcanic rocks and comparatively more significant for Group 3 subvolcanic rocks. Thus, we infer that Group 3 samples with low Ti contents were likely formed in a supra-subduction setting, originated from a mantle wedge and the melts with compositions of continental sediments. The melts might have been formed by influence of heat flow from the subducted oceanic slab and intruded back into the accretionary complex (Fig. 16e). These

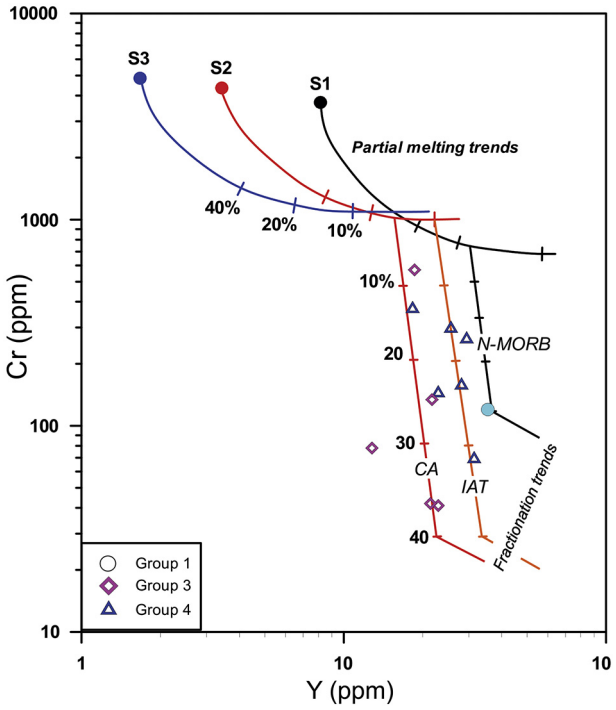


**Fig. 15.** Cr vs. Y diagram for Group 1, Group 3, and Group 4 intermediate-mafic rocks from the Tsoroidog Uul' accretionary complex (modified after Pearce 1982). N-MORB: normal mid-ocean ridge basalt, IAT: island arc tholeiitic basalt, CA: calc-alkaline.

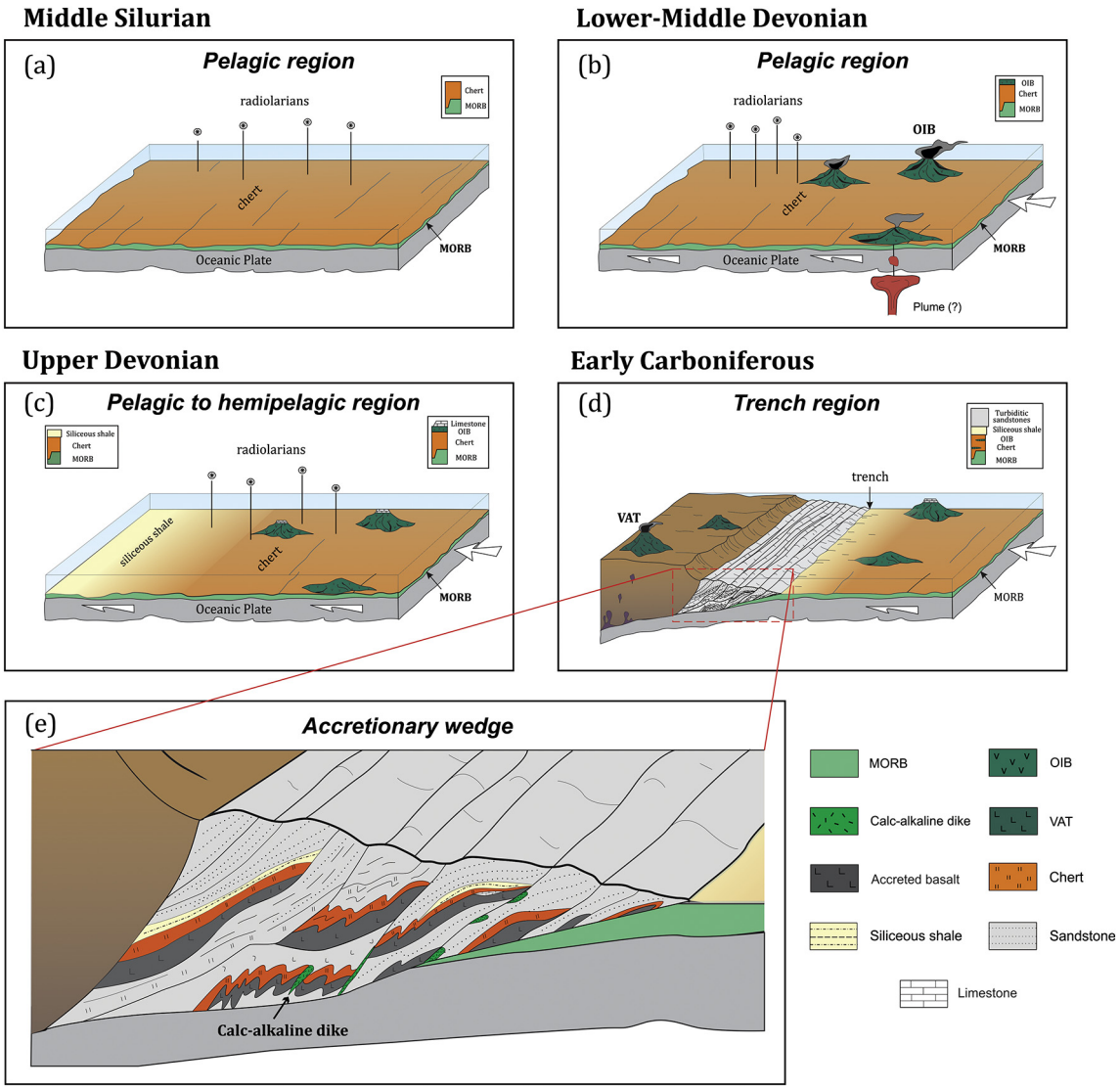


**Fig. 16.** Tectonic history of accretionary evolution between the Tsetserleg and Ulaanbaatar terranes from the Khangay-Khentey orogenic system: (a-c) spatial and temporal variations of the Paleo-Pacific Oceanic lithosphere; (d-e) provenance of the Tsoroidog Uul' accretionary complex. See Section 5.3 for discussion.

intermediate rocks are commonly observed as intruded dikes in the accretionary complex (see Section 2.2). For Group 4 rocks, samples plot in the volcanic arc field on the Th/Yb vs. Nb/Yb discrimination diagram (Fig. 11), whereas most of the samples plot in the fields of back-arc basin basalt and island arc tholeiite on the $Th_N$ vs. $Nb_N$ discrimination diagram (Fig. 12a, b). In addition, the Th enrichment relative to Nb (Fig. 10g) suggests an arc signature (Saccani et al., 2018). The overall geochemical characteristic of these rocks are quite similar to those of island arc tholeiites (Dilek et al., 2008; Saccani et al., 2011). Thus, Group 4 rocks with moderate Ti contents likely generated in afore-arc tectonic setting around the active continental margin, thus, represent volcanic arc tholeiite affinity derived from the subduction of an oceanic plate (Fig. 16d). During the subduction, oceanic islands and the fragments of MORB-type oceanic lithosphere were accreted into the continental margin, which resulted in the formation of volcanic arc tholeiites within the accretionary complex.

### 5.3. Insights to the regional tectonic evolution

According to some studies (Buchan et al., 2001, 2002; Badarch, 2005; Osozawa et al., 2008), Devonian–Carboniferous thick massive sedimentary rocks, especially those situated in the southwestern part of the Khangay-Khentey orogenic system (Fig. 1b) were accumulated within a stable sedimentary basin (known as Khangay basin) like a continental shelf (Badarch et al., 2002). Previous studies on the Khangay Group sediments considered that massive turbidite rocks can be subdivided into lower part (sandstones with "olistoliths" of radiolarian cherts and schistose meta-sandstone) and upper part (alternated sandstones and mudstones without basalt, limestone, and mélange (Kurimoto, 1997; Teraoka et al., 1996). These authors believed that the Devonian–Carboniferous sedimentary rocks of the Khangay Group represent regular coherent strata, although the main characteristic and original appearance of this stratigraphic unit is still controversial.

More recently, numerous studies suggest that the formation of the Late Silurian–Late Devonian siliceous sedimentary rocks (Kurihara et al., 2009) and thick turbidite Devonian–Carboniferous sedimentary rocks (Hara et al., 2013; Kelty et al., 2008; Suzuki et al., 2012) of the Khangay-Khentey orogenic system are an accretionary complex (Safonova et al., 2009; Safonova and Santosh, 2014; Tomurtogoo 2012; Tsukada et al., 2013) or an active continental margin of the Siberian Craton (Zorin, 1999).The accretionary complex in the Khangay-Khentey orogenic system was first investigated by researchers from Japan in the form of "Ulaanbaatar terrane" (Hara et al., 2013; Kurihara et al., 2009; Tsukada et al., 2013) according to the theory of Ocean

Plate Stratigraphy (Isozaki, 1997). In this study, our geological data from the TUAC hosted by the Tsetserleg terrane allow us to propose that this specific stratigraphic unit, consisting of oceanic components and trench-fill turbidite, is a typical accretionary complex formed by the subduction of oceanic crust (Fig. 16a–e).

We suggest that the accretionary complex of the Tsetserleg terrane, which extends into Ulaanbaatar terrane, was formed by subduction of the Paleo-Pacific Oceanic lithosphere or Mongol-Okhotsk Ocean. It was located between the Siberian Craton and Mongolia Block (also referred to as the Amuria Block) (Vander Voo et al., 2015; Wu et al., 2017b, Pan et al., 2020) and subducted under the continental margin of the Siberian Craton in the Devonian (Donskaya et al., 2013). The stratigraphic unit between those terranes are principally represented by OPS units: the upper OPS unit is represented by Lower–Upper Carboniferous Jargalant Formation with flyshoid unit and Upper Devonian–lower Carboniferous Tsetserleg Formation with turbidite unit (Erdenechimeg et al., 2018; Oyunchimeg et al., 2018), and coeval strata of these formations are the Orgioch Uul and Altanovoo Formations in the Ulaanbaatar terrane (Kelty et al., 2008; Suzuki et al., 2012). The lower to middle OPS unit is determined by Middle Silurian–Upper Devonian Erdenetsogt Formation with basalt, chert, and siliceous siltstone and shale (see Section 2.2), which are the southwestern extension of the Sergelen and Gorkhi Formations of the Ulaanbaatar terrane (Hara et al., 2013; Kurihara et al., 2009).The abovementioned formations are very similar in terms of lithology, geological structure and tectonic features and clearly display the characteristics of an accretionary complex. Considering the timing and indication of the continental flyshoid and turbidite rocks overlaying the volcanic and siliceous sedimentary rocks from the oceanic crust, the depositional age of the accretionary complex along the Tsetserleg and Ulaanbaatar terranes is proposed to be Early Carboniferous (Fig. 16d). In addition, the wide age range of cherts within the Gorkhi and Erdenetsogt Formations (spanning over 50 million years) probably indicates the existence of an extensive deep-water ocean which provided a long-lasting pelagic environment between the Siberian Craton and the North China-Tarim Blocks during the Silurian to Devonian (Fig. 16a), despite the occurrences of active sea-floor spreading and ocean plate subduction in the region (Kurihara et al., 2009) such as the Paleo-Pacific Ocean (Zonenshain et al., 1990; Zorin, 1999), the Khangai-Khantey (= Khangay Khentey) Ocean (Şengör et al., 1993; Şengör and Natal'in, 1996a, b) and the Mongol-Okhotsk Ocean (Donskaya et al., 2013; Gordienko, 2006; Tomurtogoo, 2005).

Eventually, this study characterizes the accretionary complex in the Tsetserleg terrane and confirms the relationship between the Tsetserleg terrane and Ulaanbaatar terrane as an accretion complex in the Khangay-Khentey orogenic system (Hara et al., 2013; Kurihara et al., 2009; Tsukada et al., 2013). Future investigations will expand the study on the accretionary complex (petrological study for volcanic rock, biostratigraphic study for siliceous sedimentary rock, provenance and radiometric study for turbidite sedimentary rock, as well as interpretation of lithological association and geological structure) to other accretionary terranes in the Khangay-Khentey orogenic system, according to the terrane classification of Tomurtogoo (2005, 2012). We believe that it will provide more consistent information for the subduction-accretion process along the active continental margin of the Siberian Craton and the rim of the Paleo-Pacific Ocean during Paleozoic.

## 6. Conclusions

1. Four groups of intermediate-mafic rocks from the Middle Silurian to Upper Devonian Erdentsogt Formation in the Tsoroidog Uul' accretionary complex were identified. They are associated with OPS sediments such as dark-brownish metacherts, brown-reddish cherts, limestones, whitish-gray siliceous siltstones/shales and turbidite clastic rocks.

2. Group 1 oceanic basalts formed at a mid-oceanic ridge setting with a N-MORB and *E*-MORB signatures. Group 2 basaltic rocks formed in a plume-related oceanic island setting with an OIB characteristic. Group 3 intermediate dikes were derived from a mixed source incorporating accretionary sediments and partial melting of subducted oceanic slab, formed at a supra-subduction setting with a calc-alkaline affinity. Group 4 basalts originated from refractory mantle source and formed in the fore-arc tectonic setting around an active continental margin, with volcanic arc tholeiite features.

3. The accretionary complex of the Tsetserleg terrane, which extends into Ulaanbaatar terrane, was formed by subduction of the Paleo-Pacific Oceanic lithosphere or Mongol-Okhotsk Ocean.

## Declaration of Competing Interest

The authors declare that they have no known competing financial interests or personal relationships that could have appeared to influence the work reported in this paper.

## Acknowledgements

This investigation is a result of a basic research project named "Geodynamic setting of Khangay-Khentey orogenic system and structural criteria of the gold mineralization" performed by Branch of Regional Geology and Tectonic, Institute of Geology, Mongolian Academy of Sciences from 2016 to 2018. We would like to state that this contribution is dedicated to Academician Dr. Tomurtogoo Onongo, who was a leading geologist of Mongolia and devoted his entire life to the Mongolian geology. We are grateful to Dr. Orolmaa Demberel for her valuable recommendations during the field work. We would like to thank Battushig Altanbaatar, Erdenechimeg Davaajav, Tulga Avirmed, Bulganzaya Lkhagvasuren and Ariunaa Namsrai who helped us with preparing samples for geochemical analysis and fieldwork. This study was financially supported by the Mongolian Foundation for Science and Technology (SSA_008/2013). We thank Co-Editor-in-Chief Prof. Greg Shellnutt and two anonymous referees for helpful comments.

## References

Badarch, G., 2005. Tectonic overview of Mongolia. Mongol. Geoscient. 27, 1–7.

Badarch, G., Cunningham, W.D., Windley, B.F., 2002. A new terrane subdivision for Mongolia: implication for the Phanerozoic crustal growth of Central Asia. J. Asian Earth Sci. 21, 87–110.

Buchan, B., Cunningham, D., Windley, B., Tomurhuu, D., 2001. Structural and lithological characteristics of the Bayankhongor Ophiolite Zone, Central Mongolia. J. Geol. Soc. Lond. 158, 445–460.

Buchan, C., Pfander, J., Kroner, A., Brewer, T.S., Tomurtogoo, O., Tomurhuu, D., Cunningham, D., Windley, B., 2002. Timing of accretion and collisional deformation in the Central Asian Orogenic Belt: implications of granite geochronology in the Bayankhongor Ophiolite Zone. Chem. Geol. 192, 23–45.

Bussien, D., Gombojav, N., Winkler, W., Von Quadt, A., 2011. The Mongol-Okhotsk Belt in Mongolia-an appraisal of the geodynamic development by the study of sandstone provenance and detrital zircons. Tectonophysics 510, 132–150.

Dilek, Y., Furnes, H., Shallo, M., 2008. Geochemistry of the Jurassic Mirdita Ophiolite (Albania) and the MORB to SSZ evolution of a marginal basin oceanic crust. Lithos 100, 174–209.

Donskaya, T.V., Gladkochub, D.P., Mazukabzov, A.M., Ivanov, A.V., 2013. Late Paleozoic–Mesozoic subduction-related magmatism at the southern margin of the Siberian continent and the 150 million-year history of the Mongol-Okhotsk Ocean. J. Asian Earth Sci. 62, 79–97.

Erdenechimeg, D., Oyunchimeg, T., Otgonbaatar, D., Míková, J., Tomurchudur, Ch., Dagva-Ochir, L., Enkhdalai, B., Delgerzaya, P., Sharav, D., Zavřelová, A., 2018. Geochemistry and geochronology of the Paleozoic sedimentary rocks in the Shar khutul area, Central Mongolia. Proc. Mongolian Acad. Sci. 58, 4 (228), 4–21.

Erdenesaikhan, G., Ishiwatari, A., Orolmaa, D., Aroi, Sh., Tamura, A., 2013. Middle Paleozoic greenstones of the Hangay region, central Mongolia: Remnants of an accreted oceanic plateau and forearc magmatism. J. Mineral. Petrol. Sci. 108, 303–325.

Floyd, P.A., Winchester, J.A., 1975. Magma-type and tectonic setting discrimination using immobile elements. Earth Planet. Sci. Lett. 27, 211–218.

Goldstein, S.J., Jacobsen, S.B., 1988. Nd and Sr Isotopic Systematics of River Water Suspended Material-Implications for Crustal Evolution. Earth Planet. Sci. Lett. 87, 249–265.

Gordienko, I.V., 2006. Geodynamic evolution of late Baikalides and Paleozoids in the folded periphery of the Siberian craton. Russ. Geol. Geophys. 47, 53–70.
Hara, H., Kurihara, T., Tsukada, K., Kon, Y., Uchino, T., Suzuki, T., Takeuchi, M., Nakane, Y., Manchuk, N., Minjin, C., 2013. Provenance and origins of a late Paleozoic accretionary complex within the Khangai-Khentei belt in the Central Asian Orogenic Belt, central Mongolia. J. Asian Earth Sci. 75, 141–157.
Herzberg, C., 2004. Partial melting below the Ontong Java Plateau. In: Fitton, J.G., Mahoney, J.J., Wallace, P.J., Saunders, A.D. (Eds.), Origin and evolution of the Ontong Java Plateau, Geological Society of London Special Publication, Vol. 229, pp. 179–183.
Isozaki, Y., 1997. Jurassic accretion tectonics of Japan. Island Arc 6, 25–51.
Jacobsen, S.B., Wasserburg, G.J., 1984. Sm-Nd evolution of chondrites and achondrites. Earth Planet. Sci. Lett. 67, 137–150.
Jahn, B.M., 2004. The Central Asian Orogenic Belt and growth of the continental crust in the Phanerozoic. In: Malpas, J., Fletcher, C.J.N., Ali, J.R., Aitchison, J.C. (Eds.), Aspects of the Tectonic Evolution of China, Special Publications. vol. 226. Geological Society, London, pp. 73–100.
Jahn, B.M., Wu, F.Y., Chen, B., 2000a. Granitoids of the Central Asian Orogenic Belt and continental growth in the Phanerozoic. Trans. R. Soc. Edinb. Earth Sci. 91, 181–193.
Jahn, B.M., Wu, F.Y., Chen, B., 2000b. Massive granitoid generation in Central Asia: Nd isotope evidence and implication for continental growth in the Phanerozoic. Episodes 23, 82–92.
Kelemen, P.B., Shimizu, N., Dunn, T., 1993. Relative depletion of niobium in some arc magmas and continental crust: partitioning of K, Nb, La and Ce during melt/rock reaction in the upper mantle. Earth Planet. Sci. Lett. 120, 111–134.
Kelty, T.K., Yin, A., Dash, B., Gehrels, G.E., Ribeiro, A.E., 2008. Detrital-zircon geochronology of Paleozoic sedimentary rocks in the Hangay-Hentey basin, north-central Mongolia: implications for the tectonic evolution of the Mongol- Okhotsk Ocean in Central Asia. Tectonophysics 451, 290–311.
Keto, L.S., Jacobsen, S.B., 1987. Nd and Sr isotopic variations of early Paleozoic oceans. Earth Planet. Sci. Lett. 84, 21–41.
Khain, E.V., Bibikova, E.V., Kröner, A., Zhuravlev, D.Z., Sklyarov, E.V., Fedotova, A.A., Kravchenko-Berezhnoy, I.R., 2002. The most ancient ophiolite of the Central Asian fold belt: U-Pb and Pb-Pb zircon ages for the Dunzhugur complex, Eastern Sayan, Siberia, and geodynamic implications. Earth Planet. Sci. Lett. 199, 311–325.
Kovach, V., Salnikova, E., Wang, K.-L., Jahn, B.-M., Chiu, H.-Y., Reznitskiy, L., Kotov, A., Iizuka, Y., Chung, S.-L., 2013. Zircon ages and Hf isotopic constraints on sources of clastic metasediments of the Slyudyansky high-grde complex, southeastern Siberia: implication for continental growth and evolution of the Central Asian Orogenic Belt. J. Asian Earth Sci. 62, 18–36.
Kovalenko, V.I., Yarmolyuk, V.V., Kovach, V.P., Kotov, A.B., Kozakov, I.K., Salnikova, E.B., Larin, A.M., 2004. Isotope provinces, mechanisms of generation and sources of the continental crust in the Central Asian mobile belt: geological and isotopic evidence. J. Asian Earth Sci. 23, 605–627.
Kurihara, T., Tsukada, K., Otoh, S., Kashiwagi, K., Minjin, C., Dorjsuren, B., Bujinlkham, B., Sersmaa, G., Manchuk, N., Niwa, M., Tokiwa, T., Hikichi, G., Kozuka, T., 2009. Upper Silurian and Devonian pelagic deep-water radiolarian chert from the Khangai-Khentei belt of Central Mongolia: evidence for Middle Paleozoic subduction-accretion activity in the Central Asian Orogenic Belt. J. Asian Earth Sci. 34, 209–225.
Kurimoto, C., 1997. Traveling in the Bayankhongor area in the Mongolian Steppes. Chishitsu News 509, 49–58 (in Japanese).
Le Maitre, R.W., 2002. In: Streckeisen, A., Zanettin, B., Le Bas, M.J., Bonin, B., Bateman, P., Bellieni, G., Woolley, A.R. (Eds.), Igneous Rocks: A Classification and Glossary of Terms, Recommendations of the International Union of Geological SciencesSubcommission of the Systematics of Igneous Rocks. Cambridge University Press.
Lehmann, J., Schulmann, K., Lexa, O., Corsini, M., Kröner, A., Štípská, P., Tumurhuu, D., Otgonbator, D., 2010. Structural constraints on the evolution of the Central Asian Orogenic Belt in SW Mongolia. Am. J. Sci. 310, 575–628.
Li, H., Watanabe, K., Xi, X.S., Yonezu, K., 2013. Geochemistry of volcanic rocks at Zhaokalong iron-copper-polymetallic ore deposit, Qinghai Province, China: implications for the tectonic background. Proc. Earth Planet. Sci. 6, 58–63.
Li, H., Xi, X.S., Sun, H.S., Kong, H., Wu, Q.H., Wu, C.M., Gabo-Ratio, J.A.S., 2016. Geochemistry of the Batang Group in the Zhaokalong area, Yushu, Qinghai: Implications for the late Triassic tectonism in the northern Sanjiang region, China. Acta Geol. Sin. (Eng. Ed.) 90, 704–721.
Liu, B., Wu, J.H., Li, H., Wu, Q.H., Evans, N.J., Kong, H., Xi, X.S., 2020. Geochronology, geochemistry and petrogenesis of the Dengfuxian lamprophyres: implications for the early cretaceous tectonic evolution of the South China Block. Geochemistry https://doi.org/10.1016/j.chemer.2020.125598.
Maruyama, S., Santosh, M., Zhao, D., 2007. Superplume, supercontinent, and post-perovskite: Mantle dynamics and anti-plate tectonics on the core-mantle boundary. Gondwana Res. 11, 7–37.
Maruyama, S., Kawai, T., Windley, B.F., 2010. Ocean plate stratigraphy and its imbrication in an accretionary orogen: The Mona complex, Anglesey-Lleyn, Wales, UK. In: Kusky, T.M., Zhai, M.-G., Xiao, W. (Eds.), The Evolving Conitenents: Understainding Processes of Contiental Growth, Vol. 338. Geological Society, London, Special Publications, pp. 55–75.
Orolmaa, D., Erdenesaikhan, G., 2008. Geology and geochemical characteristic of Devonian basalts from the Khangai region. Geol. Res. Treatise 18, 50–60 (In Mongolian).
Orolmaa, D., Erdenesaikhan, G., Borisenko, A.S., Fedoseev, G.S., Babich, V.V., Zhmodik, S.M., 2008. Permian-Triassic granitoid magmatism and metallogeny of the Hangayn (Central Mongolia). Russ. Geol. Geophys. 49, 534–544.
Osozawa, S., Tsolmon, G., Majigsuren, U., Jargalan, S., Niitsuma, S., Iwata, N., Pavlis, T., Jahn, B.M., 2008. Structural evolution of the Bayanhongor region, west-Central Mongolia. J. Asian Earth Sci. 33 (5), 337–352.
Oyunchimeg, T., Dagva-Ochir, L., Otgonbaatar, D., Enkh-Dalai, B., Battushig, A., 2017. New geochemical data of basalts in the Tsoroidog area, Central Mongolia. Geodyn. Tectonophys. 8 (3), 529–530.
Oyunchimeg, T., Enkhdalai, B., Otgonbaatar, D., Míková, J., Erdenechimeg, D., Sharav, D., Dagva-Ochir, L., Battushig, A., 2018. Geochemistry of the Paleozoic sedimentary rocks in the Tsoroidog Uul area from the Tsetserleg terrane: provenance and tectonic setting. Geol. Res. Treatise 24, 6–30 (in Mongolian).
Pan, Z., Appel, E., Xu, B., Turbold, S., 2020. First Paleomagnetic result from the early Permian volcanic rocks in northeastern Mongolia: evolutional implication for the Paleo-Asian Ocean and the Mongol-Okhotsk Ocean. J. Geophys. Res. Solid Earth 125 (2).
Pearce, J.A., 1982. Trace element characteristics of lavas from destructive plate boundaries. In: Thorpe, R.S. (Ed.), Andesites. Wiley, New York, pp. 525–548.
Pearce, J.A., 2008. Geochemical fingerprinting of oceanic basalts with applications to ophiolite classification and the search for Archean oceanic crust. Lithos 100, 14–48.
Purevjav, N., Roser, B., 2012. Geochemistry of Devonian-Carboniferous clastic sediments of the Tsetserleg terrane, Hangay Basin, Central Mongolia: provenance, source weathering, and tectonic setting. Island Arc 21, 270–287.
Purevjav, N., Roser, B., 2013. Geochemistry of Silurian- Carboniferous sedimentary rocks of the Ulaanbaatar terrane, Hangay-Hentey belt, Central Mongolia: Provenance, paleoweathering, tectonic setting, and relationship with the neighbouring Tsetserleg terrane. Chem. Erde 73, 481–493.
Regelous, M., Hofmann, A.W., Abouchami, W., Galer, S.J.G., 2003. Geochemistry of lavas from the emperor seamounts, and the geochemical evolution of Hawaiian magmatism from 85 to 42 Ma. J. Petrol. 44, 113–140.
Saccani, E., Principi, G., 2016. Petrological and tectonomagmatic significance of ophiolitic basalts from the Elba Island within the Alpine Corsica-Northern Apennine system. Mineral. Petrol. 110, 713–730.
Saccani, E., Beccaluva, L., Photiades, A., Zeda, O., 2011. Petrogenesis and tectono-magmatic significance of basalts and mantle peridotites from the Albanian–Greek ophiolites and sub-ophiolitic mélanges. New constraints for the Triassic–Jurassic evolution of the Neo Tethys in the Dinaride sector. Lithos 124, 227–242.
Saccani, E., Dilek, Y., Marroni, M., Pandolfi, L., 2015. Continental margin Ophiolites ofNeotethys: Remnants of Ancient Ocean-Continent transition Zone (OCTZ) Lithosphereand their Geochemistry, Mantle sources and Melt Evolution patterns. Episodes 38, 230–249.
Saccani, E., Delavari, M., Dolati, A., Marroni, M., Pandolfi, L., Chiari, M., Barbero, E., 2018. New insights into the geodynamics of Neo-Tethys in the Makran area: evidence from age and petrology of ophiolites from the Coloured Melange complex (SE Iran). Gondwana Res. 62, 306–327.
Safonova, I., Santosh, M., 2014. Accretionary complexes in the Asia-Pacific region: Tracing archives of ocean plate stratigraphy and tracking mantle plumes. Gondwana Res. 25, 126–158.
Safonova, I., Simonov, V.A., Buslov, M.M., Ota, T., Maruyama, Sh., 2008. Neoproterozoic basalts of the Paleo-Asian Ocean (Kurai accretion zone, Gorny Altai, Russia): geochemistry, petrogenesis, geodynamics. Russ. Geol. Geophys. 49, 254–271.
Safonova, I., Utsunomiya, A., Kojima, S., Nakae, S., Tomurtogoo, O., Filippov, A.N., Koizumi, K., 2009. Pacific superplume-related oceanic basalts hosted by accretionary complexes of Central Asia, Russian Far East and Japan. Gondwana Res. 16, 587–608.
Safonova, I., Buslov, M.M., Simonov, V.A., Izokh, A.E., Komiya, T., Kurganskaya, E.V., Ohno, T., 2011a. Geochemistry, petrogenesis and geodynamic origin of basalts from the Katun' accretionary complex of Gorny Altai (southwestern Siberia). Russ. Geol. Geophys. 52, 421–442.
Safonova, I., Sennikov, N.V., Komiya, T., Bychkova, Y.V., Kurganskaya, E.V., 2011b. Geochemical diversity in oceanic basalts hosted by the Zasur'ya accretionary complex, NW Russian Altai, Central Asia: implications from trace elements and Nd isotopes. J. Asian Earth Sci. 42, 191–207.
Safonova, I., Simanov, V.A., Kurganskaya, E.V., Obut, O.T., Romer, R.L., Seltmann, R., 2012. Late Paleozoic oceanic basalts hosted by the Char-suture-shear zone, East Kazakhstsan: Geological position, geochemistry, petrogenesis and tetonic setting. J. Asian Earth Sci. 49, 20–39.
Safonova, I., Maruyama, S., Kojima, S., Komiya, T., Krivonogov, S., Koshida, K., 2016. Recognizing OIB and MORB in accretionary complexes: a new approach based on ocean plate stratigraphy, petrology and geochemistry. Gondwana Res. 33, 92–114.
Safonova, I., Savinskiy, I., Perfilova, A., Gurova, A., Maruyama, S., Tsujimori, T., 2020. The itmurundy pacific-type orogenic belt in northern Balkash, central Kazakhstan: revisited plus first U-Pb age, geochemical and Nd isotope data from igneous rocks. Gondwana Res. 79, 49–69.
Schulmann, K., Paterson, S., 2011. Geodynamics: Asian continental growth. Nat. Geosci. 4, 827–829.
Şengör, A.M.C., Natal'in, B.A., 1996. Paleotectonics of Asia: fragments of a synthesis. In: Yin, A., Harrison, T.M. (Eds.), The Tectonic Evolution of Asia. Cambridge University Press, Cambridge, pp. 486–640.
Şengör, A.M.C., Natal'in, B.A., 1996a. Turkic-type orogeny and its role in the making of continental crust. Annu. Rev. Earth Planet. Sci. 24, 263–337.
Şengör, A.M.C., Natal'in, B.A., 1996b. Paleotectonics of Asia: fragments of a synthesis. In: Yin, A., Harrison, T.M. (Eds.), The Tectonic Evolution of Asia. Cambridge University Press, Cambridge, pp. 486–640.
Şengör, A.M.C., Natal'in, B.A., Burtman, V.S., 1993. Evolution of the Altaid tectonic collage and Palaeozoic crustal growth in Eurasia. Nature 364, 299–307.
Shevchenko, B.F., Popeko, L.I., Didenko, A.N., 2014. Tectonics and evolution of the lithosphere of the easthern segment of the Mongol-Okhotsk orogenic belt. Geodyn. Tectonophys. 5 (3), 667–682.
Sun, S., McDonough, W.F., 1989. Chemical and isotopic systematics of oceanic basalts: Implications for mantle composition and processes. In: Saunders, A.D., Norry, M.J. (Eds.), Magmatism in the Ocean Basins, Vol. 42. Geological Society, London, Special Publication, pp. 313–345.

Sun, H.S., Li, H., Algeo, T.J., Gabo-Ratio, J.A.S., Yang, H., Wu, J.H., Wu, P., 2019. Geochronology and geochemistry of volcanic rocks from the Tanjianshan Group, NW China: Implications for the early Palaeozoic tectonic evolution of the North Qaidam Orogen. Geol. J. 54, 1769–1796.

Suzuki, T., Nakane, Y., Bakhat, N., Takeuchi, M., Tsukada, K., Sersmaa, G., Khishigsuren, S., Manchuk, N., 2012. Description of sandstones in the Ulaanbaatar area, Mongolia. Bull. Nagoya Univ. Mus. 28, 27–38.

Takeuchi, M., Tsukada, K., Suzuki, T., Nakane, Y., Sersmaa, G., Manchuk, N., Kondo, T., Matsuzawa, N., Bakhat, N., Khishigsuren, S., Onon, G., Katsurada, Y., Hashimoto, M., Yamasaki, S., Matsumoto, A., Oyu-Erdene, B., Bulgamtsemgel, M., Kundyz, S., Enkhchimeg, L., Ganzoring, R., Myagmarsuren, G., Jamiyandagva, O., Molomjamts, M., 2012. Stratigraphy and geological structure of the Paleozoic system around Ulaanbaatar, Mongolia. Bull. Nagoya Univ. Mus. 28, 1–18.

Tatsumi, Y., 1982. Origin of the high-magnesian andesites in the Setouchi volcanic belt, Southwest Japan. Melting phase relations at high pressures. Earth Planet. Sci. Lett. 60, 305–317.

Taylor, S.T., McLennan, S.M., 1985. The Continental Crust: Composition and Evolution. Blackwell, Oxford, p. 312.

Teraoka, Y., Suzuki, M., Tungalag, F., Ichinnorov, N., Sakamaki, Y., 1996. Tectonic framework of the Bayankhongor area, west Mongolia. Bull. Geol. Surv. Japan 47, 447–455.

Togtokh, D., Gurtsoo, S., Lkhundev, Sh., Bumburuu, G., Tooruul, N., Burentugs, J., Baatar, Ts, Tomurchudur, Ch., Bilegsaikhan, Ts, Minjin, Ch., Bat-Ulzii, S., 1986. Geological Mapping Work of Scale 1:200,000 in a Region of Gurvansaikhan. Report No. 3912, Ulaanbaatar, Mongolia (Open File Report in Geological Fund of Mongolia) (in Russian).

Tomurtogoo, O., 2003. Tectonic Map of Mongolia at the Scale of 1:1,000,000, and Tectonics of Mongolia (Brief Explanatory Notes to Tectonic Map of Mongolia at the Scale of 1:1,000,000). Mineral Resources Authority of Mongolia, Ulaanbaatar.

Tomurtogoo, O., 2005. Tectonics and structural evolution of Mongolia. In: Seltmann, R., Gerel, O., Kirwin, D.J. (Eds.), Geodynamics and Metallogeny of Mongolia with a Special Emphasis on Copper and Gold Deposits. SEG-IAGOD Field Trip (14–16 August 2005), 8th Biennial SGA Meeting, IAGOD Guidebook Ser. 11: CERCAMS/NHM London, pp. 5–12.

Tomurtogoo, O., 2012. Tectonic subdivision of Mongolian orogenic domains. Geol. Res. Treatise 21, 5–25 (in Mongolian).

Tomurtogoo, O., Orolmaa, D., Erdenechimeg, D., Enkhbayar, B., Boldbaatar, G., Damdinjav, B., Taivanbaatar, Ts, Oyungerel, N., 2017. Geological Map of Mongolia at the Scale of 1: 500 000. Mineral Resources Authority of Mongolia, Ulaanbaatar.

Tsukada, K., Nakane, Y., Yamamoto, K., Kurihara, T., Otoh, S., Kashiwagi, K., Minjin, C., Sersmaa, G., Manchuk, N., Niwa, M., Tokiwa, T., 2013. Geological setting of basaltic rocks in an accretionary complex, Khangai-Khentei Belt, Mongolia. Island Arc 22, 227–241.

Ufland, A.K., Filippova, I.B., 1967. L-47 Geological Sheet Maps of Scale 1:1,000,000, Moscow. Report No. 1761-f (Open File Report in Geological Fund of Mongolia) (in Russian).

Van der Voo, R., Van Hinsbergen, D.J.J., Domeier, M., Spakman, W., Torsvik, T.H., 2015. Latest Jurassic-earliest Cretaceous closure of the Mongol-Okhotsk Ocean: A paleomagnetic and seismological-tomographic analysis. In: Anderson, T.H., Didenko, A.N., Johnson, C.L., Khanchuk, A.I., MacDonald Jr., J.H. (Eds.), Late Jurassic Margin of Laurasia-A Record of Faulting Accommodating Plate Rotation. Geological Society of America Special Paper 513, pp. 589–606.

Wang, T., Huang, C., Du, G., Liu, Y., Xie, J., Li, H., 2019. Geochronology, geochemistry and zircon Hf-isotopes of the early Mesoproterozoic Yaopengzi dolerite in SW Yangtze block (Sichuan, SW China): implications for the Columbia supercontinent breakup. Geosci. J. 23 (4), 557–573.

Weaver, B.L., 1991. The origin of ocean island basalts and member compositions: trace element and isotopic constrains. Earth Planet. Sci. Lett. 104, 381–397.

Wilhem, C., Windley, B.F., Stampfli, G.M., 2012. The Altaids of Central Asia: a tectonic and evolutionary innovative review. Earth-Sci. Rev. 113, 303–341.

Windley, B.F., Alexeiev, D., Xiao, W., Kroner, A., Badarch, G., 2007. Tectonic models for accretion of the central Asian orogenic belt. J. Geol. Soc. Lond. 164, 31–47.

Workman, R.K., Hart, S.R., 2005. Major and trace element composition of the depleted MORB mantle (DMM). Earth Planet. Sci. Lett. 231, 53–72.

Wu, L., Kravchinsky, V.A., Potter, D.K., 2017a. Apparent polar wander paths of the major Chinese blocks since the late Paleozoic: toward restoring the amalgamation history of east Eurasia. Earth-Sci. Rev. 171, 492–519.

Wu, J.H., Li, H., Xi, X.S., Kong, H., Wu, Q.H., Peng, N.L., Wu, X.M., Cao, J.Y., Gabo-Ratio, J.A.S., 2017b. Geochemistry and geochronology of the mafic dikes in the Taipusi area, northern margin of North China Craton: Implications for Silurian tectonic evolution of the Central Asian Orogen. J. Earth Syst. Sci. 126, 64. https://doi.org/10.1007/s12040-017-0841-z.

Xiao, W., Windley, B.F., Hao, J., Zhai, M.-G., 2003. Accretion leading to collision and the Permian Solonker suture, Inner Mongolia, China: termination of the central Asian orogenic belt. Tectonics 22 (6), 1069.

Xiao, W., Windley, B.F., Badarch, G., Sun, S., Li, J., Qin, K., Wang, Z., 2004. Palaeozoic accretionary and convergent tectonics of the southern Altaids: implications for the growth of Central Asia. J. Geol. Soc. Lond. 161, 339–342.

Yarmolyuk, V.V., Kovalenko, V.I., Kozlovsky, A.M., Kovach, V.P., Sal'nikova, E.B., Kovalenko, D.V., Kotov, A.B., Kudryashova, E.A., Lebedev, V.I., Eenzhin, G., 2008. Crust-forming processes in the Hercynides of the Central Asian Foldbelt. Petrology 16, 679–709.

Yarmolyuk, V.V., Kovach, V.P., Kozakov, I.K., Kozlovsky, A.M., Kotov, A.B., Rytsk, E.Y., 2012. Mechanisms of continental crust formation in the Central Asian foldbelt. Geotectonics (4), 3–27.

Zonenshain, L.P., Kuzmin, M.I., Natapov, L.M., 1990. Geology of the USSR: a plate tectonic synthesis. American Geophysical Union, Geodynamics Series 21, p. 242.

Zorin, Y.A., 1999. Geodynamics of the western part of the Mongolia-Okhotsk collisional belt, Trans-Baikal region (Russia) and Mongolia. Tectonophysics 306, 33–56.